

1 An improved global land cover mapping in 2015 with 30 2 m resolution (GLC-2015) based on a multi-source product 3 fusion approach

4 Bingjie Li ¹, Xiaocong Xu ¹, Xiaoping Liu ^{1,2}, Qian Shi ¹, Haoming Zhuang ¹, Yaotong
5 Cai ¹ and Da He ¹

6 ¹School of Geography and Planning, Sun Yat-Sen University, Guangzhou, 510275, China

7 ²Southern Marine Science and Engineering Guangdong Laboratory (Zhuhai), Zhuhai, 519080, China

8 *Correspondence to:* Xiaoping Liu (liuxp3@mail.sysu.edu.cn)

9 **Abstract.** Global land cover (GLC) information with fine spatial resolution is a fundamental data input
10 for studies on biogeochemical cycles of the Earth system and global climate change. Although there are
11 several public GLC products with 30 m resolution, considerable inconsistencies were found among them
12 especially in fragmented regions and transition zones, which brings great uncertainties to various
13 application tasks. In this paper, we developed an improved global land cover map in 2015 with 30 m
14 resolution (GLC-2015) by fusing multiple existing [land cover \(LC\)](#) products based on the Dempster-
15 Shafer theory of evidence (DSET). Firstly, we used more than 160,000 global point-based samples to
16 locally evaluated the reliability of the input GLC products for each land cover class within each 4°×4°
17 geographical grid for the establishment of the basic probability assignment (BPA) function. Then, the
18 Dempster's rule of combination was used for each 30 m pixel to derive the combined probability mass
19 of each possible land cover class from all the candidate maps. Finally, each pixel was determined with a
20 land cover class based on a decision rule. Through this fusing process, each pixel is expected to be
21 assigned with the land cover class that contributes to achieve a higher accuracy. We assessed our product
22 separately with 34,711 global point-based samples and 201 global patch-based samples. Results show
23 that, the GLC-2015 map achieved the highest mapping performance globally, continentally, and eco-
24 regionally compared with the existing 30 m GLC maps, with an overall accuracy of 79.5% (83.6%) and
25 a kappa coefficient of 0.757 (0.566) against the point-based (patch-based) validation samples.
26 Additionally, we found that the GLC-2015 map showed substantial outperformance in the areas of

27 inconsistency, with an accuracy improvement of 19.3%-28.0% in areas of moderate inconsistency, and
28 27.5%-29.7% in areas of high inconsistency. Hopefully, this improved GLC-2015 product can be applied
29 to reduce uncertainties in the research on global environmental changes, ecosystem service assessments,
30 and hazard damage evaluations, etc. The GLC-2015 map developed in this study is available at
31 <https://doi.org/10.6084/m9.figshare.22358143.v2> (Li et al., 2022).

32 **1. Introduction**

33 Land cover (LC), influenced by both nature and human activities (Running, 2008; Gong et al., 2013;
34 Song et al., 2018; Liu et al., 2021a), is a significant component of the Earth system (Yang and Huang,
35 2021). Global land cover (GLC) products can serve as fundamental data for various studies, such as
36 climate and environmental changes (Bounoua et al., 2002; Foley et al., 2005; Grimm et al., 2008; Yang
37 et al., 2013; Schewe et al., 2019), food security (Verburg et al., 2013; Ban et al., 2015), carbon cycling
38 (Moody and Woodcock, 1994; Defries et al., 2002; Gómez et al., 2016), biodiversity conservation
39 (Chapin et al., 2000; Giri et al., 2005) and land management (Mayaux et al., 2004; Verburg et al., 2011).
40 Therefore, there is a pressing need for detailed, accurate, and high-quality GLC product to support global
41 change research and sustainable development.

42 In the preliminary stage, LC mapping mainly relied on visual interpretation, which is time-
43 consuming, labor-intensive and difficult to be applied at the global scale (Gong, 2012). In recent decades,
44 satellite remote sensing data, which can provide information of large area coverage and long-term
45 monitoring, has been adopted to generate GLC products. With coarse resolution satellite data such as
46 Advanced Very High Resolution Radiometer (AVHRR), Moderate Resolution Imaging
47 Spectroradiometer (MODIS), Medium Resolution Imaging Spectrometer (MERIS), and Global Land
48 Surface Satellite (GLASS), a variety of GLC products have been developed at 5 km to 300 m
49 resolution (Loveland et al., 2000; Hansen et al., 2000; Bartholomé and Belward, 2005; Friedl et al., 2010;
50 Defourny et al., 2018; Liu et al., 2020a). Although these GLC products have been widely applied to many
51 applications, it has been proved that the differences between sensors, classification systems, and
52 considerably low accuracies in areas prevent harmonization of these products (Herold et al., 2008;
53 Verburg et al., 2011; Grekousis et al., 2015). Also, these products are far from providing enough fine
54 spatial details of LC due to their relatively coarse spatial resolution, which does not meet the demand of

55 many studies (Giri et al., 2013; Yang et al., 2017). To allow researches which can capture most human
56 activity, finer-resolution (e.g., 30 m) GLC products are demanded (Giri et al., 2013).

57 With the free accessibility of high-resolution satellite remote sensing data, GLC mapping at fine
58 resolution has been successfully conducted. Using Landsat imagery, there has been a milestone
59 achievement that the two GLC products are generated with fine resolution of 30 m, namely Finer
60 Resolution Observation and Monitoring of Global Land Cover product (FROM_GLC)(Gong et al., 2013)
61 and Globeland30 (Chen et al., 2015). After that, a 30 m-resolution GLC mapping in 2017 was achieved
62 using the first all-season sample set (Li et al., 2017). More recently, Zhang et al. (2021) used both Landsat
63 time series imagery and high-quality training data from the Global Spatial Temporal Spectra Library
64 (GSPECLib) to produce a 30 m GLC map in 2015 (GLC_FCS30) with a two-level classification scheme.
65 Several attempts have been made to improve accuracy of 30 m GLC products which are prevail in the
66 generation of GLC mapping task over the last few years. FROM_GLC was created by employing four
67 classification algorithms to classify the Landsat images and choosing time series of MODIS EVI data for
68 training and test. Globeland30 was created by proposing a pixel-object-knowledge-based (POK) method
69 to assure consistency and accuracy. GLC_FCS30 was generated by adopting local adaptive random forest
70 models with high-quality training samples derived from GSPECLib. The Globeland30, FROM_GLC,
71 and GLC_FCS30 are excellent and indispensable GLC products which have contributed much to various
72 researches, such as biodiversity conservation (Wu et al., 2020; Meng et al., 2023), climate change (Kim
73 et al., 2016; Xue et al., 2021; Zheng et al., 2022), and land management (Shafizadeh-Moghadam et al.,
74 2019). [In addition to these multiple-class GLC products, GLC products for individual LC classes, such
75 as cropland \(Yu et al., 2013; Lu et al., 2020\), forest \(Hansen et al., 2013; Shimada et al., 2014; Zhang et
76 al., 2020\), wetland \(Hu et al., 2017; Zhang et al., 2023\), water bodies \(Liao et al., 2014; Pekel et al., 2016;
77 Pickens et al., 2020\), and impervious surfaces \(Gong et al., 2020; Huang et al., 2021; Huang et al., 2022;
78 Liu et al., 2020b\), have been successfully generated.](#)

79 Despite the great efforts in producing more accurate products, the existing 30 m GLC products still
80 show unstable performance in certain LC classes and some specific areas (Sun et al., 2016; Kang et al.,
81 2020). Furthermore, the existing 30 m products showed great agreement in overall spatial distribution
82 patterns but significant spatial inconsistency in some specific areas (heterogeneous areas and transition
83 zones) and spectrally similar classes (forest and shrubland, cropland and grassland) (Gao et al., 2020;

84 Liu et al., 2021b). The spatial inconsistency between the existing 30m GLC products are resulted from
85 differences in their classification systems, classification techniques employed, source data, and spatial
86 distribution and size of training samples (Yang et al., 2017; Gao et al., 2020). Due to the aforesaid
87 limitations, users of GLC products still have difficulties in an appropriate selection of data for their
88 specific application. Ultimately, this situation leads to uncertainties in outcomes of related researches
89 when different 30 m GLC products are used. For GLC mapping with fine spatial resolution, more efforts
90 should be focused on improving the mapping in heterogenous and fragmented landscape (Herold et al.,
91 2008; Liu et al., 2021b). Therefore, it is pressing to generate a more accurate and reliable GLC product
92 with high classification accuracy, especially for spatially inconsistent regions and low-accuracy LC
93 classes.

94 According to Gong et al. (2016), inconsistencies between LC products indicate available
95 complementary information and more robust and reliable data can be generated by integrating the input
96 maps with the data fusion method. Given that different maps have disagreement and provide accurate
97 information in different locations, we can make a best choice for the class label assigned to each pixel
98 by weighting the credibility of all the available information and combining them through a decision rule
99 (Clinton et al., 2015). In this way, the output map of integration on input maps can reduce the overall risk
100 of assigning a wrong class label to a pixel and at least achieve the average performance of input maps.
101 Several attempts have been made to produce an accurate and consistent LC map using various methods,
102 such as majority voting (MV), fuzzy agreement and Bayesian theory. Iwao et al. (2011) created a GLC
103 map based on a simple majority voting method. Jung et al. (2006) generated a 1km GLC map by
104 combination of MODIS, GLC2000 and GLCC data based on fuzzy agreement scoring. Subsequently,
105 Fritz et al. (2011) extended the synergy method of Jung et al. (2006) by ranking LC maps and mapped
106 the cropland extent in Sub-Saharan Africa. See et al. (2015) generated two GLC products by integrating
107 medium resolution LC products with geographically weighted regression (GWR). Gengler and Bogaert
108 (2018) proposed a Bayesian data fusion method and applied it to the LC mapping for a specific region in
109 Belgium. All these researches have demonstrated that fusion method can create an integrated LC product
110 where the mapping accuracy is greatly improved by combing the best of candidate maps. However, the
111 MV method is sensitive to the quality of the candidate maps and has significant uncertainties when the
112 input products exhibit great disagreement (Chen and Venkataramanan, 2005). The fuzzy agreement is

113 highly subjective since it depends on expert assessment, while the Bayesian theory requires a prior
114 knowledge or conditional probabilities and fails to handle the states of ignorance (Liu and Xu, 2021).

115 The Dempster-Shafer theory of evidence (DSET) is an evidence-based approach to reason with
116 uncertainties. Unlike the majority voting, the DSET method can discount evidence from inaccurate
117 information with a probability mass that reflects the degree of belief rather than a binary decision (Razi
118 et al., 2019). In contrast to the Bayesian theory, the DSET can integrate evidence from a variety of sources
119 without the requirement of prior knowledge (Chen and Venkataramanan, 2005). Moreover, the reliability
120 of the final fused results based on the DSET method is measured with a total degree of belief. Although
121 previous literatures focused on the application of the DSET method in multisource data aggregation, very
122 little research has been conducted at a global scale due to the lack of accurate and sufficient samples and
123 the demand for adequate computing resources.

124 In this research, we propose a multi-source product fusion approach on the Google Earth Engine
125 (GEE) platform to produce an improved GLC product in 2015 (GLC-2015) with 30 m resolution. The
126 fusion approach we proposed aims to deal with the inconsistency between previous 30 m GLC products
127 and generate a map which has better mapping performance than any of the candidate maps by evaluating
128 the mapping accuracy of these existing products at the local scale and choosing the most credible LC
129 class. To fulfill the purpose, we first performed reliability evaluation, where the accuracy of each GLC
130 product for each LC class in each $4^\circ \times 4^\circ$ geographical grid is regarded as the evidential probability to
131 create the basic probability assignment (BPA) function. Then, the BPA values of all the LC classes from
132 different GLC products were fused according to the Dempster's rule of combination. Finally, the GLC-
133 2015 map was integrated after a final accepted LC class with the maximum combined probability mass
134 was assigned to each 30 m pixel. The GLC-2015 map was separately validated with two different
135 validation sets, namely global point-based samples and global patch-based samples, and compared with
136 three existing multiple-class GLC products. Moreover, we provided an analysis for the mapping
137 improvement of the GLC-2015 compared to other products in areas of high mapping inconsistency. The
138 GLC-2015 map is proved to be accurate and credible and can significantly improve the mapping accuracy
139 in areas of high inconsistency.

140 **2. Datasets**

141 **2.1 Multiple-class GLC products**

142 Three existing 30m GLC products with multiple classes, including GlobeLand30, FROM_GLC and
143 GLC_FCS30, were employed as input maps in the fusion based on DSET. A summary of their detailed
144 information is shown in Table 1.

145 GlobeLand30, a widely-used global geo-information product, was produced by the POK-based
146 method using Landsat and HJ-1 satellite images. Globeland30 products are freely accessible online at
147 the website (<http://www.globalland30.org>) for 2000 and 2010. From the accuracy assessment, the
148 Globeland30 for the year 2010 had an overall accuracy exceeded 80% using large samples (Chen et al.,
149 2015). Although the data time of GlobeLand30 is 2010, which has a five-year gap with other products,
150 it was used because the changed areas of LC caused by the time interval are tiny compared to the global
151 land area. In addition, there is relatively less uncertainty due to LC changes than due to inaccurate
152 classification (Xu et al., 2014). Most spatial disagreements between the existing maps are about
153 classification errors rather than LC changes over the time interval (Mccallum et al., 2006; See et al.,
154 2015).

155 FROM_GLC was first generated using numerous Landsat images, which has a fine classification
156 system with a two-level structure. It achieved an OA of 64.5% through validation with the complete test
157 samples and 71.5% with a subset of test samples in homogeneous areas (Gong et al., 2013). We used the
158 version of 2015 for the fusion.

159 GLC_FCS30 was developed using Landsat time series data and large training samples from the
160 GSPECLib. It has a two-level classification scheme that contains 16 global LCCS LC classes and 14
161 detailed regional LC classes. The overall accuracy of the GLC_FCS30 according to LCCS level-1
162 validation scheme reached 71.4% (Zhang et al., 2021).

163 **Table 1. Detailed information of GLC products and national-scale LC products used in this paper.**

Product name	Satellite sensors	Year of reference	Access	Literature
Globeland30	Landsat TM/ETM+ HJ-1 A/B	2010	http://www.globallandcover.com/	(Chen et al., 2015)
FROM_GLC	Landsat TM/ETM+/OLI	2015	http://data.ess.tsinghua.edu.cn/	(Gong et al., 2013)

GLC_FCS30	Landsat OLI	2015	https://doi.org/10.5281/zenodo.3986872	(Zhang et al., 2021)
GAUD	Landsat TM/ETM+/OLI	2015	https://doi.org/10.6084/m9.figshare.11513178.v1	(Liu et al., 2020c)
GFC	Landsat TM/ETM+	2015	http://earthenginepartners.appspot.com/science-2013-global-forest	(Hansen et al., 2013)
JRC GSW	Landsat TM/ETM+/OLI	2015	http://global-surface-water.appspot.com/	(Pekel et al., 2016)
GMW	ALOS PALSAR Landsat TM/ETM+	2015	https://data.unep-wcmc.org/datasets/45	(Bunting et al., 2018)
NLCD 2016	Landsat TM / OLI	2016	https://www.mrlc.gov/data/nlcd-2016-land-cover-conus	(Yang et al., 2018)
CLUD	HJ-1 CBERS-1	2015	/	(Liu et al., 2014)
CLCD	Landsat TM/ETM+/OLI	2015	https://doi.org/10.5281/zenodo.4417810	(Yang and Huang, 2021)

164 2.2 Single-class GLC products

165 To improve the quality of the fusing result, a set of highly qualified GLC products with single class at 30
166 m fine resolution were also used. Compared to the multiple-class GLC products, these single-class GLC
167 products are more likely to provide accurate information since they usually focus on promoting mapping
168 performance of specific LC class. These products include Global Forest Change (GFC) (Hansen et al.,
169 2013), Global Annual Urban Dynamics (GAUD) (Liu et al., 2020b), Joint Research Centre's Global
170 Surface Water (JRC GSW) (Pekel et al., 2016), and Global Mangrove Watch (GMW) (Bunting et al.,
171 2018). While these single-class products are either annual or multi-epoch, we only selected these
172 products in the target year of 2015. The background information of these single-class products was
173 considered as another land cover class (e.g., non-water) participating in the fusion. The accuracy of the
174 background information was defaulted to 0 since it did not provide information about any of the other
175 nine categories in our classification system. Table 1 also describes the information of these selected
176 single-class GLC products.

177 GFC was resulted from a time-series analysis of growing season Landsat scenes, aiming to provide

178 information about global tree cover extent, gain, and loss at a 30m spatial resolution. The accuracy
179 assessment was performed at global and climate domain scales and the forest gain reached an overall
180 accuracy of 99.6% and forest loss reached 99.7% across the globe (Hansen et al., 2013). Up to now, it
181 has a temporary coverage from 2000 to 2020.

182 GAUD, which provides 30m annual urban extent for the time period of 1985 to 2015, was generated
183 using numerous Landsat images with both data fusion approach and temporal segmentation approach on
184 the GEE platform. Validation was conducted across different urban ecoregions and the globe by the
185 product developer. The accuracy of mapping urbanized year was 76% for the period of 1985 to 2000 and
186 82% for the period of 2000 to 2015 at humid regions worldwide (Liu et al., 2020c).

187 JRC GSW dataset provides a monthly presentation of global surface water changes from 1984 to
188 2015 at a fine 30 m resolution. Expert systems, visual analytics and evidential reasoning were exploited
189 to detect water extent and changes. Based on 40,124 validation points over the globe and across the 32
190 years, commission accuracies were determined with overall accuracies of 99.45% (TM), 99.35% (ETM+)
191 and 99.54% (OLI) and omission accuracies were reflected in overall accuracies of 97.01% (TM), 95.79%
192 (ETM+) and 96.25%(OLI) (Pekel et al., 2016). We used the GSW Yearly Water Classification History
193 v1.1 in the GEE catalog. A single 'waterClass' band is present in each image that provides the water's
194 seasonality throughout the year with four types: no data, no water, seasonal water, and permanent water.
195 Since the seasonal water in GSW data is not as reliable as the permanent water (Meyer et al., 2020), we
196 selected permanent water bodies and excluded seasonal water bodies.

197 GMW dataset was produced as a result of the GMW initiative, which aims to provide consistent
198 information of mangrove extent. The global mangrove map in 2010 was generated as a baseline map
199 employing the Extremely Randomized Trees classifier to classify ALOS PALSAR and Landsat imagery.
200 Assessed by a total of 53,878 sample points globally, the overall accuracy of the baseline map reached
201 95.3% and the producer's accuracy achieved 94.0% (Bunting et al., 2018). Based on the baseline in 2010,
202 mangrove extent maps for six epochs between 1996 and 2016 have been established and annual change
203 monitoring from 2018 and onwards are undertaken.

204 **2.3 National-scale LC products**

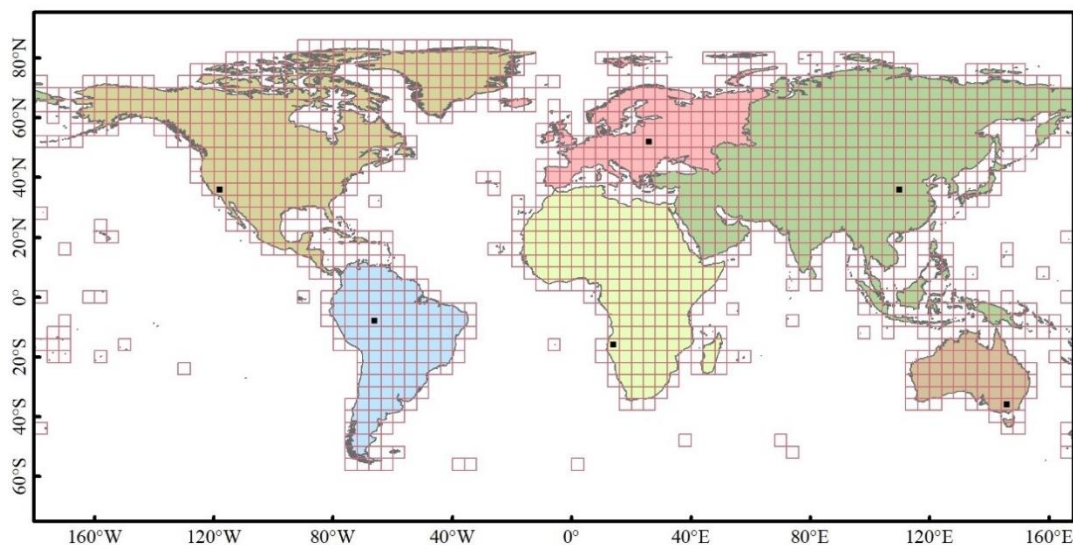
205 Land cover products which focus on a national scale are more likely to possess higher accuracy
206 because they were produced by experts who have good knowledge of land cover classes nationally. Thus,

207 the National Land Cover Database 2016 (NLCD 2016) for the year 2016 [over the conterminous United](#)
208 [States \(CONUS\)](#) (Yang et al., 2018), China’s land-use/cover dataset (CLUD) (Liu et al., 2014) for 2015,
209 and the annual China land cover dataset (CLCD) (Yang and Huang, 2021) for 2015 were also included
210 in the fusion. The detailed information of these national-scale products was listed in Table 1.

211 NLCD 2016 database, which provides continuous and accurate information about land cover and
212 change from 2001 to 2016 at an interval of 2 or 3 years, was produced based on a pixel- and object-based
213 approach and an effective post-classification process (Yang et al., 2018). The level-1 and level-2 overall
214 accuracy of NLCD 2016 database for 2016 was 90.6% and 86.4% for CONUS, respectively (Wickham
215 et al., 2021). CLUD, developed by the digital interpretation method using Landsat images, provide land
216 cover information over China from 1980s to 2015. The overall accuracy of CLUD reached 94.3% and
217 91.2% for level-1 and level-2 land cover classes, respectively (Liu et al., 2014). CLCD was generated
218 with stable training samples derived from CLUD and Landsat time series. Assessed with 5463 validation
219 samples, CLCD obtained an overall accuracy of 79.31% (Yang and Huang, 2021).

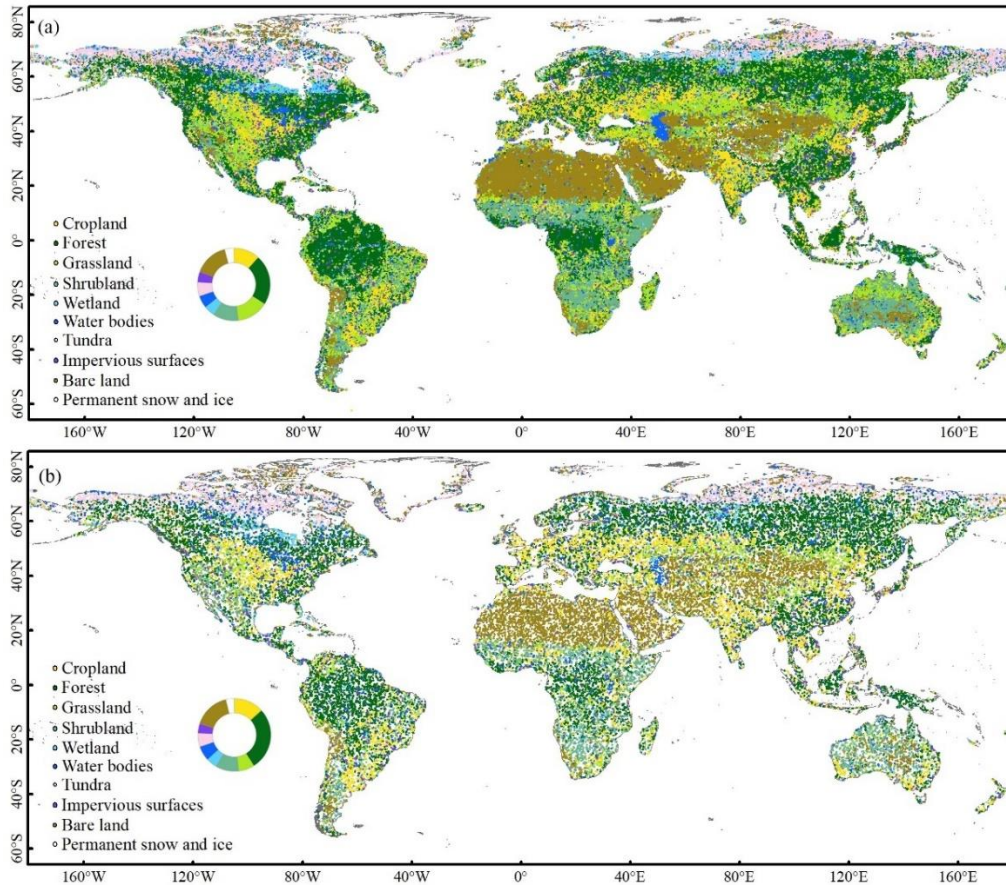
220 2.4 Global point-based and patch-based samples

221 In this study, we collected two sets of global samples, namely the global point-based samples and the
222 global patch-based samples. To collect representative and sufficient samples efficiently, we divided the
223 world’s terrestrial area into $4^\circ \times 4^\circ$ geographical grids. A total of 1,507 grids are distributed evenly across
224 the globe, shown as Figure 1.



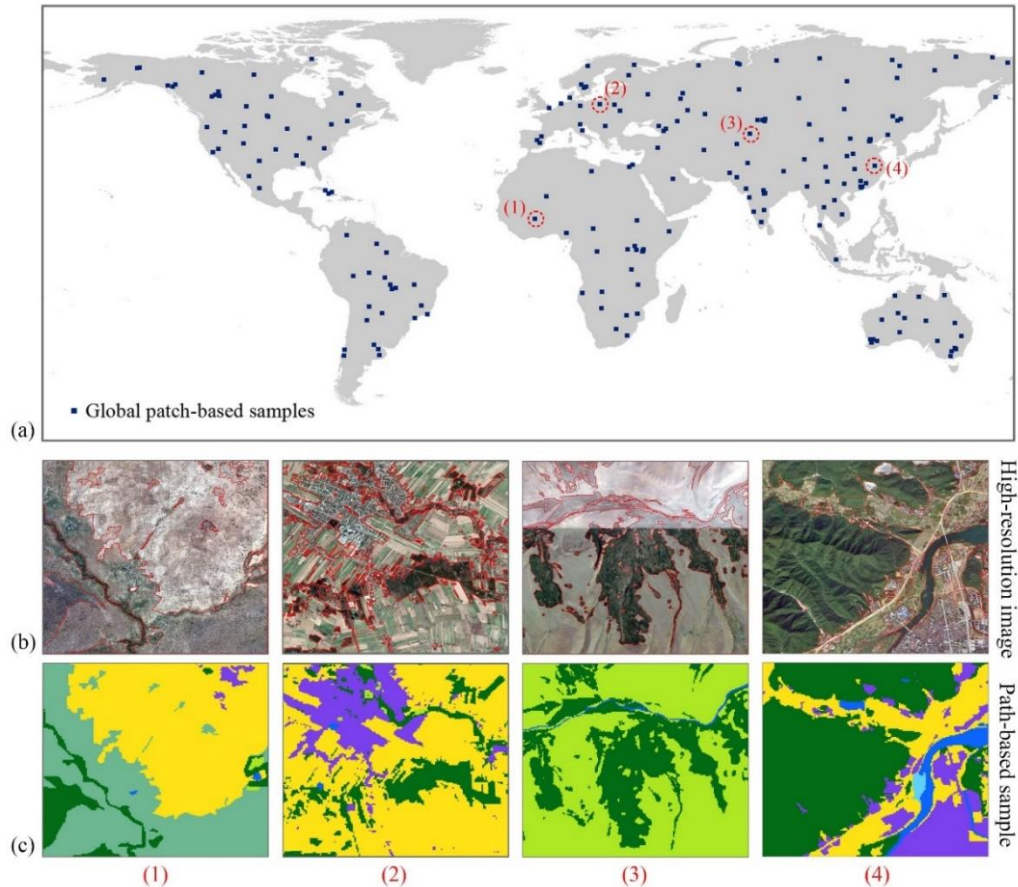
225
226 **Figure 1. Spatial distribution of the $4^\circ \times 4^\circ$ geographical grids over the world. Six black rectangle tiles with**
227 **size of 0.25° were used for visual comparison between our product and other three products.**

228 To derive the global point-based samples, we adopted stratified random sampling in each grid. The
229 stratified random sampling depends on area ratio of LC classes from a LC product. We used the
230 FROM_GLC as prior knowledge rather than the Globeland30 and GLC_FCS30 with two considerations:
231 (1) the FROM_GLC has the same data time as our target map (GLC-2015) while the Globeland30 has a
232 5-year interval from our samples, which affects the size of samples for each LC class; (2)the 10 level-1
233 land cover classes of the FROM_GLC is similar to that in the classification system of the GLC-2015,
234 while the GLC_FCS30 has differences with the GLC-2015 in the classification scheme and definition of
235 land cover classes. First, the FROM_GLC product was used to calculate the area ratio of each LC class.
236 Then, points were randomly extracted from the FROM_GLC according to the area ratio and spatial
237 location of each class. Finally, more than 200,000 global samples were collected. Through the sampling
238 method mentioned above, the global point-based samples were even across the globe and sufficient for
239 each LC class in each grid. Therefore, more than 50 points could be easily derived for LC classes with a
240 small area ratio in the $4^{\circ} \times 4^{\circ}$ grid. The FROM_GLC shows low accuracy for some LC classes, especially
241 for cropland and forest (Gao et al., 2020; Liu et al., 2021b; Zhang et al., 2021; Zhang et al., 2022). If the
242 global samples were extracted with LC class label from the FROM_GLC, there would be inevitable
243 errors. Therefore, the FROM_GLC was only used to determine the size and location of samples for each
244 LC class. Instead, all the points were manually labeled according to Google Earth high-resolution images.
245 The whole sample set was randomly split into two subsets: 80% of the global samples were used to assess
246 the accuracy of each GLC product for various LC classes at the global scale and in each grid. The
247 remaining 20% were used for the validation of the GLC-2015 map and data inter-comparison between
248 different GLC products. Figure 2 presents the distribution of the whole global point-based samples and
249 the subset for accuracy assessment and data inter-comparison.



250
 251 **Figure 2. Spatial distribution of (a) the global point-based samples, (b) the subset of the global point-based**
 252 **samples for accuracy assessment and data inter-comparison, the proportions of each LC class are shown in**
 253 **the pie chart.**

254 To verify the consistency between the GLC-2015 and the actual pattern of the landscape at the local
 255 scale, we also established the global patch-based samples. Simple random sampling was used to derive
 256 5 km × 5 km blocks over the world's terrestrial area and across different ecoregions because it is easy to
 257 perform and capable to augment the sample size from target areas (Pengra et al., 2020). Since
 258 inconsistency between current GLC maps tends to appear in those heterogeneous areas, such as
 259 fragmented regions and transition zones, we slightly increased the sample size for areas with the
 260 heterogeneous landscape to better evaluate our mapping results. In total, there were 201 blocks selected
 261 as the global patch-based samples, as displayed in Figure 3a. Then, for each block in the patch-based
 262 samples, we used ArcGIS 10.5 software to derive polygons (patches) of various sizes which captured the
 263 real landscape on the high-resolution images. Meanwhile, each polygon was manually labeled with a LC
 264 class. Four examples of producing patch-based samples are shown in Figure 3b, c.

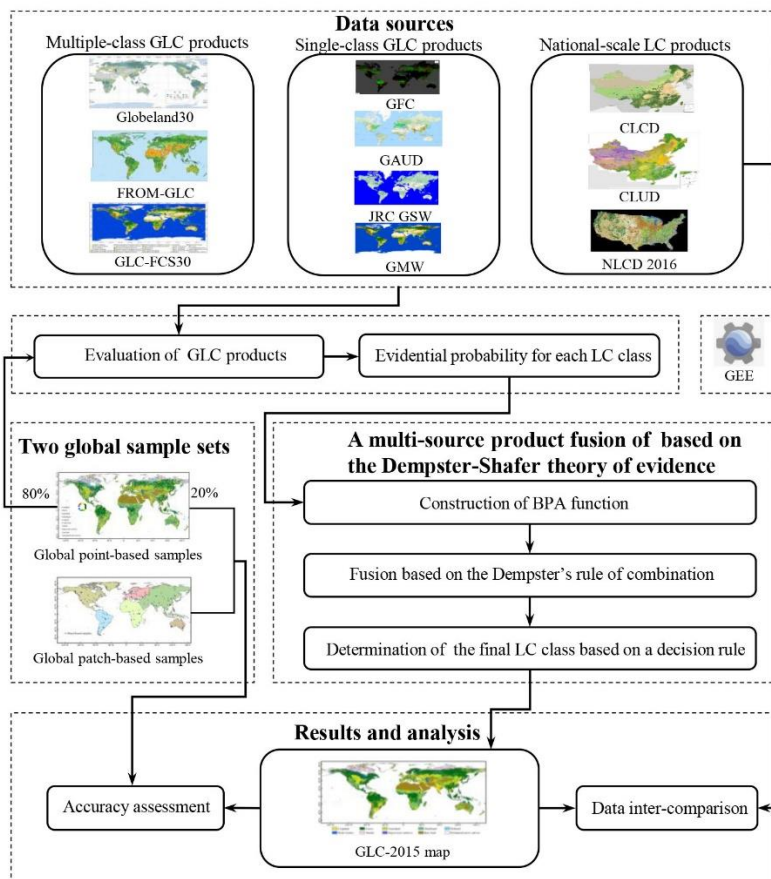


265
 266 **Figure 3. Spatial distribution and selected examples of the global patch-based samples. The location of 5 km**
 267 **× 5 km patch-based samples are shown as panel (a), the locations of four selected samples are remarked by**
 268 **red dash circles. Panels (b) and (c) illustrate the production of global patch-based samples on manual**
 269 **interpretation. The red lines in high-resolution images circa 2015 are results after vectorization using ArcGIS**
 270 **10.5 software. Four corresponding patch-based samples are shown as (c).**

271 3. Methods

272 In this study, we proposed a multi-source product fusion method to produce the GLC-2015 map. The
 273 procedure mainly comprised the fusion based on the Dempster-Shafer theory of evidence (DSET),
 274 accuracy assessment and data inter-comparison (Figure 4). The basic of this study is the fusion of multi-
 275 source GLC products based on DSET. The fusion method was performed at the pixel level and it involves
 276 the following three main steps: (1) Construct the basic probability assignment (BPA) function of each
 277 pixel that belongs to each LC class considering the accuracy assessment of different GLC products; (2)
 278 calculate the combined probability mass for each class per pixel using the Dempster's rule of combination;
 279 and (3) determine the finally accepted LC class per pixel by a decision rule. Afterwards, pixels with a
 280 determined LC class were integrated to generate a new map. For large-scale or global land cover mapping,

281 previous researchers divided the study area into a lot of sub-regions and conducted classification in each
 282 sub-region on GEE (Gong et al., 2020; Liu et al., 2020c; Huang et al., 2021; Jin et al., 2022; Zhang et al.,
 283 2021; Zhao et al., 2021). The shape and size of sub-region vary in previous work, such as hexagons with
 284 a side length of 2° , geographical grids with a size of $1^\circ \times 1^\circ$, $3.5^\circ \times 3.5^\circ$, $5^\circ \times 5^\circ$, or $10^\circ \times 10^\circ$. When deciding
 285 on the size of sub-regions, two important factors should be considered. The size of samples in each sub-
 286 region should be sufficient so that the rare land cover classes will not be missed. On the other hand, it is
 287 impossible to implement mapping work at a sub-region as larger as we want due to memory constraints.
 288 To determine the appropriate size, we tested different sizes of the sub-region (see Table S1). Result shows
 289 that dividing the study area into $4^\circ \times 4^\circ$ grids performed best. Therefore, we split the world's terrestrial
 290 area into 1507 $4^\circ \times 4^\circ$ geographical grids. The entire framework was implemented in all $4^\circ \times 4^\circ$
 291 geographical grids on the GEE platform.



292
 293 **Figure 4. The framework for generating the GLC-2015 map using a multi-source product fusion approach**
 294 **based on DEST.**

295 **3.1 Definition of the classification system**

296 In this study, we adopted the classification system with 10 LC classes, including cropland, forest,

297 grassland, shrubland, wetland, water bodies, tundra, impervious surfaces, bare land, and permanent snow
 298 and ice (Chen et al., 2015), as listed in Table 2. Due to the applications for different social needs, the
 299 existing GLC products and national-scale LC products were produced with different classification
 300 systems (Tables S2-S3). The GlobeLand30 used a simple classification system that only contained 10
 301 first-level classes. Unlike the GlobeLand30, the FROM_GLC and GLC_FCS30 were classified with a
 302 two-level classification scheme. Through analysis of these systems, we found that the classification
 303 systems are not the same, but they have some agreements. There are both 10 major classes in the
 304 GlobeLand30 and FROM_GLC despite that the definition of some classes differs. Additionally, in
 305 contrast to the GlobeLand30 and FROM_GLC, the level-0 classification system of the GLC_FCS30
 306 lacks tundra. However, in the level-2 detailed LC classes of the GLC_FCS30, lichens and mosses has
 307 little distinction with tundra.

308 **Table 2. Classification system adopted in this paper.**

Id	LC class	Definition
10	Cropland	Land areas used for food production and animal feed.
20	Forest	Land areas dominated by trees with tree canopy cover over 30%, and sparse trees with tree canopy cover between 10%-30%.
30	Grassland	Land areas dominated by natural grass with a cover over 10%.
40	Shrubland	Land areas dominated by shrubs with a cover over 30%, including mountain shrubs, deciduous shrubs, evergreen shrubs and desert shrubs with a cover over 10%.
50	Wetland	Land areas dominated by wetland plants and water bodies.
60	Water bodies	Land areas covered with accumulated liquid water.
70	Tundra	Land areas dominated by lichen, moss, hardly perennial herb and shrubs in the polar regions.
80	Impervious surfaces	Land areas covered with artificial structures.
90	Bare land	Land areas with scarce vegetation with a cover lower than 10%.
100	Permanent snow and ice	Land areas dominated by permanent snow, glacier and icecap.

309 According to the LC translation tables (Tables S2-S3), the original LC classes of FROM_GLC and
 310 GLC_FCS30, CLUD for 2015, and NLCD 2016 for 2016 were converted into the 10 target land cover
 311 classes based on the similarity of LC definition. Note that cropland in our classification system was
 312 defined as land areas for food production and animal feed. Therefore, pasture in level-2 classes of the

313 FROM_GLC was converted into cropland rather than grassland. In addition, lichens/mosses in the level-
 314 2 detailed LC classes of GLC_FCS30 was converted into tundra.

315 **3.2 A multi-source product fusion for the GLC-2015 mapping**

316 The DSET is an effective method widely applied for the fusion of multi-source data. To generate a new
 317 high-quality GLC map, a multi-source product fusion method using DSET was proposed. In the
 318 remainder of the section 3.2, We introduced the overview on the theory and presented the application of
 319 DSET in our mapping process.

320 **3.2.1 Dempster-Shafer theory of evidence**

321 The DSET is developed by Dempster and Shafer, which is an extension of Bayesian probability theory.
 322 This theory treats information from different data sources as independent evidence and integrated these
 323 evidences with no requirements regarding the prior knowledge. In the fusion, we assume a classification
 324 process in which all the input data are to be classified into mutually exclusive classes. Let the set Ω of
 325 these classes be a frame of discrimination. 2^Ω is the power set of Ω that includes all the classes and
 326 their possible unions. We defined the function $m: 2^\Omega \rightarrow [0,1]$ as the basic probability assignment (BPA)
 327 function if and only if it satisfies $m(\emptyset) = 0$ and $\sum_{A \in 2^\Omega} m(A) = 1$ with \emptyset denotes an empty set. For
 328 each class $A \subseteq 2^\Omega$, $m(A)$ is called the basic probability mass which can be computed from the BPA
 329 function and represents the degree of support for class A or confidence in class A.

330 The purpose of fusion is to evaluate and integrate information from multiple sources. In the DSET,
 331 these multi-source data are regarded as different evidence and provide different assessments. To generate
 332 all the evidences, Dempster-Shafer theory of evidence offers a rule. Suppose $m_i(B_j)$ is the basic
 333 probability mass computed from the BPA function for each input data i with $1 \leq i \leq n$ for all classes
 334 $B_j \in 2^\Omega$. Dempster's rule of combination is provided to calculate a combined probability mass from
 335 different evidences. The fusion rules are given in equation (1) and (2).

$$336 \quad m(C) = \frac{\sum_{B_1 \cap B_2 \dots \cap B_n = C} \prod_{1 \leq i \leq n} m_i(B_j)}{1 - k} \quad (1)$$

337

$$338 \quad k = \sum_{B_1 \cap B_2 \dots \cap B_n = \emptyset} \prod_{1 \leq i \leq n} m_i(B_j) \quad (2)$$

339 Where k represents the basic probability mass associated with conflicts among the sources of evidence.

340 C is the intersection of all classes B_j and carries the joint information from all the input data. After the
 341 combination, we took a decision rule to decide the class we finally accept. There are several ways to
 342 decide the final class by simply choosing the class with the maximum belief, plausibility, support, or
 343 commonality.

344 3.2.2 Mapping based on DSET

345 Here, we presented our implementation for the GLC-2015 mapping in the framework of DSET. All the
 346 multiple-class and single-class GLC products described in Sect. 2 were selected as input maps to be
 347 combined. In the integration of multi-source GLC products, since all the LC classes in our classification
 348 system are known, the frame of discrimination was defined to be our classification system:

$$349 \quad \Omega = \left\{ \begin{array}{l} \text{cropland, forest, grassland, shrubland, wetland, water bodies,} \\ \text{tundra, impervious surfaces, bare land, permanent snow and ice} \end{array} \right\} \quad (3)$$

350 The definition of BPA function is the critical point in applying DSET (Rottensteiner et al., 2005).
 351 In the fusion, we wanted to achieve a per-pixel classification into one of ten LC classes: cropland, forest,
 352 grassland, shrubland, wetland, water bodies, tundra, impervious surfaces, bare land, and permanent snow
 353 and ice. For each single-class or multiple-class GLC product, the accuracy for each LC class was
 354 calculated and used as evidential probability to construct the BPA. Given that the local accuracy for a
 355 $4^\circ \times 4^\circ$ grid was not able to adequately reflect the actual land cover landscape, especially for the rare LC
 356 classes, the global accuracy was incorporated into the construction of the BPA to avoid uncertainties from
 357 a local point of view. Since the assessment based on local samples plays a more critical role in BPA
 358 construction for a local grid, a higher weight should be assigned to the local accuracy. To identify the
 359 best weight, we tested different weights of the local accuracy (see Figure S1). The result shows that using
 360 75% performed robustly and obtained relatively higher overall accuracy. Therefore, we chose 75% as
 361 the weight for local accuracy and 25% for global accuracy. Here, we defined the BPA function as follow:

$$362 \quad m_i(T_j) = \frac{PA_{local(ij)} + UA_{local(ij)}}{2} \times 75\% + \frac{PA_{global(ij)} + UA_{global(ij)}}{2} \times 25\% \quad (4)$$

363 Where $m_i(T_j)$ represents the BPA function of evidence source i for the LC class T_j ; $PA_{local(ij)}$,
 364 $UA_{local(ij)}$ denote producer's accuracy and user's accuracy of evidence source i for the LC class T_j for
 365 each $4^\circ \times 4^\circ$ geographical grid, respectively; $PA_{global(ij)}$, $UA_{global(ij)}$ denote producer's accuracy and
 366 user's accuracy of evidence source i for LC class T_j at the global scale.

367 To estimate the exact values of $PA_{local(ij)}$, $UA_{local(ij)}$, $PA_{global(ij)}$ and $UA_{global(ij)}$, we used 80%

368 of the global point-based samples more than 160,000 points derived in Sect 2.3. As soon as we obtained
 369 the measurements of $m_i(T_j)$, the combined probability masses $m(T_j)$ were evaluated based on
 370 Dempster's rule of combination for each pixel classified as the LC class T_j by fusing BPA values of all
 371 the evidence sources:

$$372 \quad m(T_j) = \frac{1}{1-k} \sum_{T_{1j} \cap T_{2j} \dots \cap T_{nj} = T_j} m_i(T_j) \quad (5)$$

$$373 \quad k = \sum_{T_{1j} \cap T_{2j} \dots \cap T_{nj} = \emptyset} m_i(T_j) \quad (6)$$

374 Where k represents the basic probability mass associated with conflict; $m_i(T_j)$ represents the basic
 375 probability mass of a certain pixel belonging to the LC class T_j from different GLC products.

376 Additionally, a belief measure (Bel) was given to measure the degree of credibility that a pixel
 377 labeled as the finally accepted LC class when combining all the available evidences. The belief measure
 378 was determined by

$$379 \quad Bel(T_j) = \sum_{T_{ij} \subseteq T_j} m_i(T_j) \quad (7)$$

380 To determine the finally accepted LC class per pixel, we took the rule of maximum combined
 381 probability mass as our decision rule and the LC class with the maximum combined probability mass is
 382 assigned to the 30 m pixel. Pixels labeled with the LC class were integrated to generate the GLC-2015
 383 product.

384 **3.3 Accuracy assessment**

385 To assess the accuracy of the GLC-2015 map, we utilized two validation methods: validation with the
 386 global point-based samples and the global patch-based samples. Since the global point-based sample set
 387 is distributed evenly across the world and its sample size for each LC class is relatively sufficient and
 388 balanced, even for the rare classes, it can provide a representative and credible basis for estimation of the
 389 GLC-2015 map globally. Furthermore, we used the global patch-based samples to conduct accuracy
 390 assessment from the local landscape scale. Although the global patch-based sample set provide an
 391 inadequate sample size for rare LC classes, it can take advantage of the spatial context information and
 392 efficiently reflect the actual pattern of the landscape.

393 The confusion matrix was produced to evaluate and analyze the GLC-2015 mapping result. The
 394 error matrix is composed of entry A_{ij} , which represents the number of samples with reference LC class

395 j being classified as LC class i . The overall accuracy (OA), kappa coefficient, producer's accuracy (PA),
 396 and user's accuracy (UA) were generated from confusion matrix to describe the quality of the GLC-2015
 397 map. They are defined as follows:

$$398 \quad OA = \frac{\sum_i A_{ii}}{\sum_i \sum_j A_{ij}} \quad (8)$$

$$399 \quad P_o = OA \quad (9)$$

$$400 \quad P_e = \sum_k \frac{\sum_i A_{ik}}{\sum_i \sum_j A_{ij}} \times \frac{\sum_j A_{kj}}{\sum_i \sum_j A_{ij}} \quad (10)$$

$$401 \quad kappa = \frac{P_o - P_e}{1 - P_e} \quad (11)$$

$$402 \quad PA^i = \frac{A_{ii}}{\sum_k A_{ki}} \quad (12)$$

$$403 \quad UA^i = \frac{A_{ii}}{\sum_k A_{ik}} \quad (13)$$

404 Where UA^i and PA^i represent UA and PA of the LC i , respectively; P_o is the agreement between the
 405 reference and the classified data; P_e is the hypothetical probability of chance agreement.

406 3.4 Data inter-comparison

407 To better reflect the quality of the GLC-2015 map, we intercompared the GLC-2015 map with the
 408 existing LC products at multiple scales. In the accuracy assessment of different products, two global
 409 validation sets described earlier were employed.

410 To figure out whether the GLC-2015 map promotes accuracy in the areas with high classification
 411 difficulty and how much the improvement is compared to the existing products, we conducted the spatial
 412 consistency analysis between the GlobeLand30, FROM_GLC, and GLC_FCS30 and compared the
 413 mapping performance of the GLC-2015 with others in the areas of low inconsistency, moderate
 414 inconsistency, and high inconsistency. To visually present the spatial consistency between three existing
 415 GLC maps, we employed the spatial superposition method to obtain the spatial correspondence pixel-
 416 by-pixel between different maps. Based on the times of all the GLC products agreed for the same LC
 417 class, the degree of consistency for a pixel was identified as three levels with the agreement value equal
 418 to 3, 2, or 1. The areas of low inconsistency were regarded as pixels that classified as the same LC class
 419 in all three GLC maps (labeled as 3). The moderate inconsistency areas were regarded as pixels that were
 420 consistent in only two GLC maps (labeled as 2). The high inconsistency areas were regarded as pixels
 421 that were totally inconsistent in these three GLC maps (labeled as 1). For a visual comparison, all these

422 GLC maps were aggregated to 0.05° , in which the LC class with the largest proportion determined the
423 class in each 0.05° grid.

424 **3.5 Assessment on mapping performance of DSET and other methods**

425 In addition to inter-comparison between the GLC-2015 map and three existing GLC products, we
426 compared the DSET method with two existing commonly used fusion methods, including the majority
427 voting (MV) and spatial correspondence (SC) based on two global validation sets including 20% of the
428 global point-based samples and the whole global patch-based samples. MV is a fusion approach that
429 combines input maps and adopts the LC class favored by the majority of the candidate maps. In the MV
430 method, we compared the GlobeLand30, FROM_GLC, and GLC_FCS30 at each pixel and chose the
431 class that two or three LC products agreed for. For pixels where three LC products were different, the
432 LC class of the product with the highest accuracy was adopted. SC method produces an integrated land
433 cover map by selecting the LC class of the input map that has the highest spatial correspondence with
434 the reference data. In this study, 80% of the global point-based samples were used as the reference data
435 to obtain the SC map of each global LC product. If the class of a product agreed with that of the point-
436 based sample, a value equal to 1 was assigned to that sample. On the contrary, a value equal to 0 was
437 assigned to the sample if the class of the product differed from that of the sample. In each $4^\circ \times 4^\circ$ grid,
438 we used the Kriging method to obtain spatial correspondence maps which have the correspondence value
439 ranging from 0 to 1 for three products. Then, the class of the product with the highest spatial
440 correspondence was chosen for each pixel.

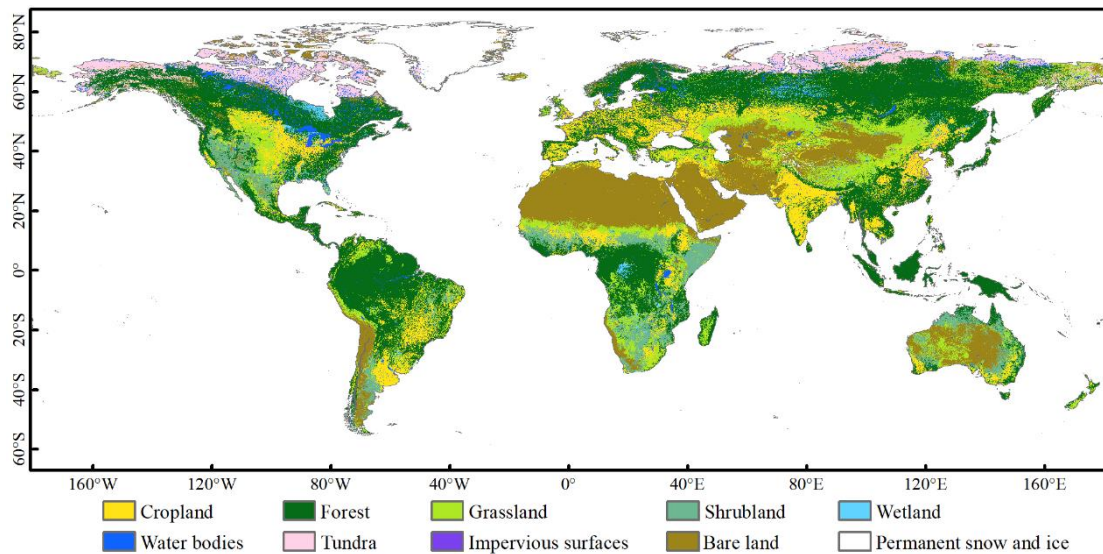
441 Furthermore, we compared the mapping performance of DSET with Random Forest (RF) which is
442 considered one of the most popular algorithms for land cover mapping. In the land cover classification
443 using the FR classifier, all available Level-2 Tier 1 surface reflectance (SR) data of Landsat 8 OLI
444 (Operational Land Imager) sensors from the year 2015 and two adjacent years on GEE was employed.
445 All Landsat images have been atmospherically corrected. The following six bands were used as input
446 features: blue, green, red, NIR, SWIR1, and SWIR2. To improve the mapping performance, several
447 important spectral indices, including DNVI, NDWI, and NDBI were also used as auxiliary data to the
448 RF classifier. The RF classifier was trained on 80% of the global point-based samples since those samples
449 were of high quality after manual visual interpretation of high-resolution images. As the global land cover
450 mapping based on the RF classifier is a tough task, we randomly selected a total of 300 grids with the

451 size of 4° (Figure S2) and applied corresponding local RF classifiers to these grids. Then, the mapping
452 results were validated by the remaining 20% of the point-based samples.

453 4. Results and discussion

454 4.1 Mapping result of the GLC-2015 map

455 Using a multi-source product fusion method based on the DSET, we generated an improved 30m global
456 land cover map in 2015 (GLC-2015). Figure 5 illustrates the GLC-2015 map. The GLC-2015 map can
457 accurately describe the spatial distribution of various LC classes. For example, cropland areas are mostly
458 located in Central America, the region from the Hungarian plain to the Siberian plain, the eastern and
459 southern parts of China, and the most of India. In addition, forest, which is one of the easily
460 distinguishable classes from the map, is concentrated in the eastern part of North America, the Amazon
461 basin of South America, the northern part of Eurasia and the equatorial region of Africa.



462

463 **Figure 5. Global land cover map in 2015 with 30 m resolution (GLC-2015).**

464 4.2 Accuracy assessment of the GLC-2015 map

465 4.2.1 Accuracy assessment with the global point-based samples

466 The accuracy of the GLC-2015 map was first tested via the global point-based samples, and the results
467 of assessment are listed in Table 3. The GLC-2015 map achieved an OA of 79.5% and kappa coefficient
468 of 0.757 at the global scale, demonstrating the good performance of our map. Among all the LC classes,
469 permanent snow and ice possessed the best mapping performance, with PA and UA achieving 89.1% and

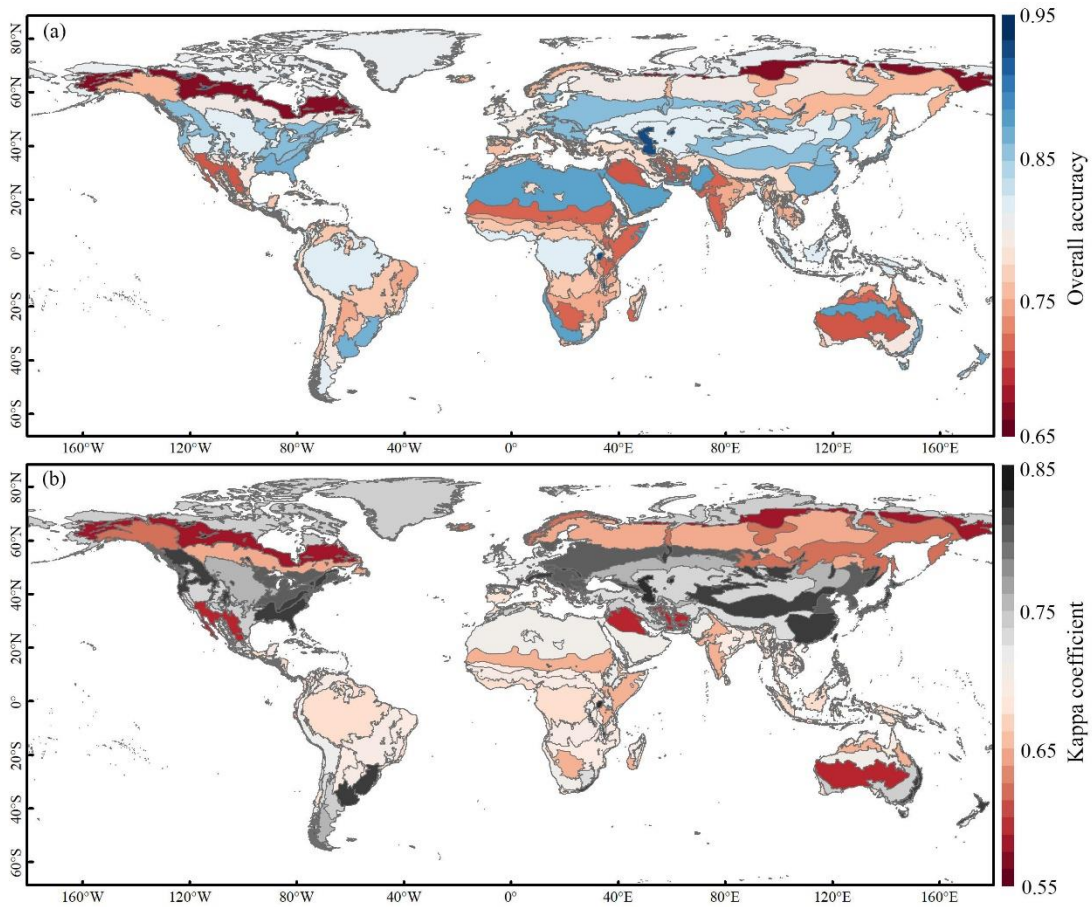
470 93.7%. The accuracy of water bodies, forest and impervious surfaces was also high, where PA and UA
 471 exceeded 80.0%. Grassland, shrubland, and wetland had relatively low accuracy, with PA below 75.0%.
 472 Among them, grassland and shrubland were mainly confused with forest, which might be because these
 473 classes are both vegetation, thus causing difficulty in recognition by spectral information. Due to the
 474 complex spectral characteristics, wetland is often mixed with vegetation (Ludwig et al., 2019).

475 **Table 3. The confusion matrix for the GLC-2015 map based on the global point-based samples.**

	Cropland	Forest	Grassland	Shrubland	Wetland	Water bodies	Tundra	Impervious surfaces	Bare land	Permanent snow and ice	Total	PA
Cropland	3623	387	356	61	27	48	2	71	81	0	4656	0.778
Forest	155	8813	186	141	232	16	43	43	53	3	9685	0.910
Grassland	10	337	1920	19	24	13	47	36	184	9	2599	0.739
Shrubland	155	438	656	1469	39	29	70	78	442	4	3380	0.435
Wetland	47	287	82	14	1067	64	22	18	110	4	1715	0.622
Water bodies	27	90	15	1	73	1936	17	10	44	3	2216	0.874
Tundra	1	242	119	6	29	19	1411	2	269	17	2115	0.667
Impervious surfaces	74	41	11	3	8	11	1	1295	45	0	1489	0.870
Bare land	36	59	237	32	44	91	55	60	4909	38	5561	0.883
Permanent snow and ice	0	11	8	0	4	18	13	1	86	1154	1295	0.891
Total	4128	10705	3590	1746	1547	2245	1681	1614	6223	1232	34711	
UA	0.878	0.823	0.535	0.841	0.690	0.862	0.839	0.802	0.789	0.937		
OA						0.795						
Kappa						0.757						

476 The regional accuracies are presented in Figure 6. The OA of the GLC-2015 ranged from 66.4% to
 477 93.4%, and kappa coefficient from 0.552 to 0.813. From the perspective of OA, Water regions lead,
 478 followed by Tropical desert, Temperate continental forest, and Polar. These are areas with homogeneous
 479 land cover and have low difficulty in mapping. Boreal tundra woodland, Tropical dry forest, Tropical
 480 shrubland, and Subtropical desert are the regions with low OA. The first one may be related to the high
 481 latitudes. The followed two may be because they belong to areas with complicated and mixed LC classes
 482 which is not easily classified. The last one may be the consequence of sparse vegetation in desert areas.

483 For the kappa coefficient, the ranking was similar with those for OA.



484
485 **Figure 6. Regional accuracy of the GLC-2015 map according to ecoregions. (a)overall accuracy, (b) kappa**
486 **coefficient. The ecoregion boundaries are obtained from the Food and Agriculture Organization of the United**
487 **Nations (FAO).**

488 4.2.2 Accuracy assessment with the global patch-based samples

489 The accuracy assessment of the GLC-2015 map was also conducted with the global patch-based samples.
490 Table 4 summarizes the results for accuracy assessment of each LC class in the GLC-2015 map. From
491 the assessment results, it can be found that the OA of the GLC-2015 map reached 83.6%, which was
492 higher than 79.5% tested with the global point-based samples. The kappa coefficient of the GLC-2015
493 map was 0.566, which was 0.191 lower than the result calculated with the global point-based samples.
494 In both accuracy assessment results based on two different validation data sets, water bodies, forest, and
495 permanent snow and ice were validated to have high accuracy, and grassland, shrubland, and wetland
496 were validated to have low accuracy. Nevertheless, the ranking of accuracy for each LC class had a slight
497 difference. For example, in assessment based on the global point-based samples, impervious surfaces
498 and permanent snow and ice ranked higher than that based on the global patch-based samples. This may

499 be because a LC map can easily show where one LC class is distributed but hardly describe its actual
500 shape. In addition to the accuracy assessment on a pixel scale, validation on a patch scale is equally
501 important because it can reflect the shape consistency between the GLC-2015 map and the actual
502 landscape, even if the size of global patch-based samples is relatively small. Overall, no matter from the
503 perspective of the global point-based samples or the global patch-based samples, the mapping accuracies
504 of the GLC-2015 map are satisfactory.

505 **Table 4. Mapping accuracy via the global patch-based samples for the GLC-2015 map**

	Cropland	Forest	Grassland	shrubland	Wetland	Water bodies	Tundra	Impervious surfaces	Bare land	Permanent snow and ice
PA	0.887	0.895	0.629	0.589	0.301	0.939	0.701	0.757	0.682	0.825
UA	0.916	0.844	0.617	0.714	0.511	0.917	0.872	0.713	0.599	0.767
OA							0.836			
Kappa							0.566			

506 **4.3 Inter-comparison with existing GLC products**

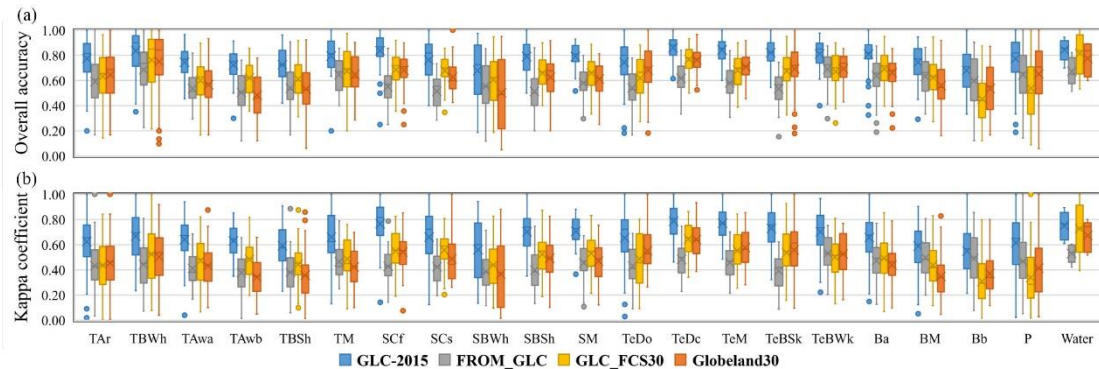
507 **4.3.1 Inter-comparison based on the global point-based samples**

508 Based on the global point-based samples, the inter-comparison of the GLC-2015 map with the
509 GlobeLand30, FROM_GLC, and GLC_FCS30 were conducted. Since the three products used different
510 classification systems, LC classes were transformed to the classification system we adopted in this paper
511 to achieve consistent accuracy assessment. The accuracy assessment results for all GLC maps are listed
512 in Table 5. It can be found that the GLC-2015 map achieved the highest OA of 79.5% compared with
513 GlobeLand30 of 65.3%, FROM_GLC of 61.7%, and GLC_FCS30 of 65.5%, respectively. The accuracy
514 gap between the GLC-2015 map and other existing ones was 14.0%-17.8%. Also, the GLC-2015 map
515 possessed a better kappa coefficient than other products. For each LC class, the GLC-2015 map
516 outperformed the other three maps in terms of PA except for tundra. For cropland, grassland, shrubland,
517 wetland, and tundra, the GLC-2015 map also exhibited better performance for UA than the GlobeLand30,
518 FROM_GLC and GLC_FCS30. Overall, for the PA or UA, the GLC-2015 map ranked first or second in
519 nearly all LC classes, which demonstrated that the GLC-2015 map had smaller omission and commission
520 errors against the other three products.

521 **Table 5. Mapping accuracy of the GLC products with the global point-based samples.**

		Cropland	Forest	Grassland	Shrubland	Wetland	Water bodies	Tundra	Impervious surfaces	Bare land	Permanent snow and ice	OA (Kappa coefficient)
GLC-2015	PA	0.778	0.910	0.739	0.435	0.622	0.874	0.667	0.870	0.883	0.891	0.795
	UA	0.878	0.823	0.535	0.841	0.690	0.862	0.839	0.802	0.789	0.937	(0.757)
Globeland30	PA	0.752	0.719	0.713	0.245	0.540	0.680	0.769	0.688	0.609	0.821	0.653
	UA	0.786	0.818	0.255	0.428	0.573	0.869	0.577	0.809	0.868	0.905	(0.598)
FROM_GLC	PA	0.389	0.694	0.707	0.411	0.307	0.607	0.712	0.732	0.731	0.881	0.617
	UA	0.671	0.859	0.278	0.422	0.289	0.742	0.686	0.661	0.761	0.773	(0.558)
GLC_FCS30	PA	0.757	0.775	0.452	0.399	0.455	0.604	0.228	0.777	0.809	0.726	0.655
	UA	0.616	0.816	0.384	0.405	0.515	0.808	0.688	0.774	0.645	0.947	(0.591)

522 Further quantitative accuracy assessments of different GLC products were performed in $4^{\circ} \times 4^{\circ}$
523 grids using the global point-based samples, and box plots were produced for each product for all grids
524 within different ecoregions, as shown in Figure 7. It can be found that the GLC-2015 map outperformed
525 other existing products with the best OA and kappa coefficient across different ecoregions. Also, the
526 mean overall accuracy of the GLC-2015 map exceeded 65.0% in all ecoregions, showing the high quality
527 of our mapping results. It is worth noting that the GLC-2015 map showed shorter boxes except in
528 Subtropical dry forest and Subtropical desert, which means the GLC-2015 map had relatively small
529 fluctuation than other ones. In Subtropical desert, Tropical dry forest, and Boreal tundra woodland, the
530 OA and kappa coefficient of the four products were relatively low. However, the GLC-2015 map
531 exceeded the highest of others and greatly improved the mean OA in these regions.



532
533 **Figure 7. The box-plot of the accuracy for twenty-one ecoregion zones. (a) overall accuracy, (b)kappa**
534 **coefficient. Ecoregion abbreviation and corresponding ecoregion is described in Table S4.**

535 **4.3.2 Inter-comparison based on the global patch-based samples**

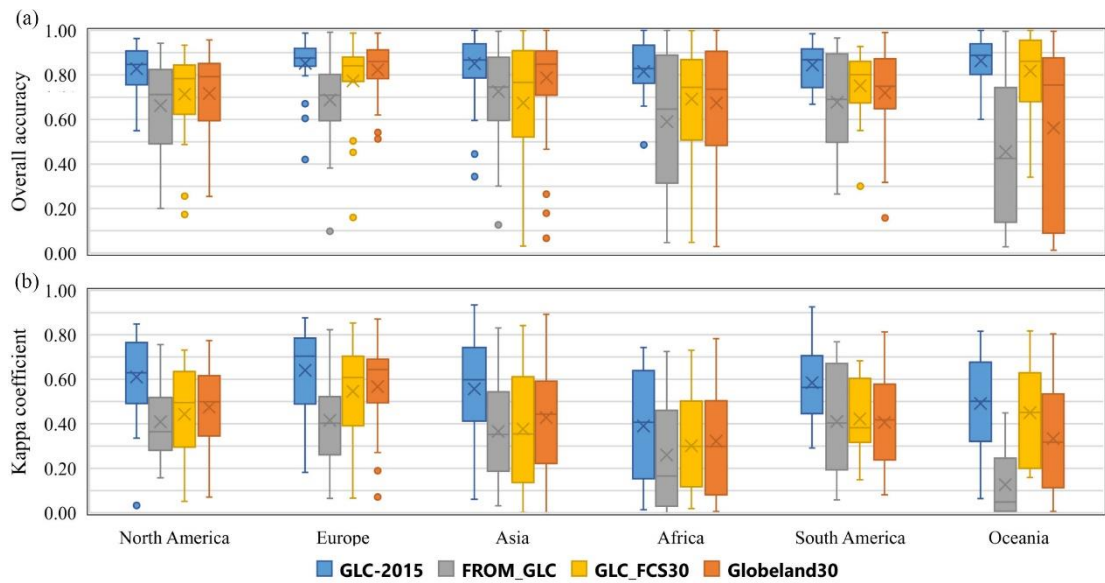
536 Although the global point-based samples are adequate and even across the globe, the distribution of
 537 points in each $4^\circ \times 4^\circ$ geographical grid is too sparse to reflect the actual spatial pattern of the landscape.
 538 Focusing on LC pattern at the local scale, we also used the global patch-based samples which can provide
 539 spatial context information to conduct the accuracy assessment of the GLC-2015 map and compare
 540 difference GLC products. Table 6 lists the accuracies of the GLC-2015 map and the other three GLC
 541 products. Obviously, the GLC-2015 map achieved the best OA and kappa coefficient among these four
 542 GLC maps. The overall accuracy gap between the GLC-2015 product and others was 5.9%-24.5%, which
 543 presented a more significant variation compared with the result based on the global point-based samples.
 544 In terms of PA and UA, the GLC-2015 map was higher than the other three ones in most LC classes.
 545 Specifically, all the products had lower accuracy for grassland, shrubland, and wetland, similar to that in
 546 the accuracy assessment based on the global point-based samples. It is evident that the FROM_GLC had
 547 the lowest mapping accuracy for grassland, shrubland, and wetland, implying that the classification
 548 method of FROM_GLC is not robust for these three LC classes.

549 **Table 6. Mapping accuracy of the GLC products with the global patch-based samples**

		Cropland	Forest	Grassland	Shrubland	Wetland	Water bodies	Tundra	Impervious surfaces	Bare land	Permanent snow and ice	OA
GLC-2015	PA	0.887	0.895	0.629	0.589	0.301	0.939	0.701	0.757	0.682	0.825	0.836
	UA	0.916	0.844	0.617	0.714	0.511	0.917	0.872	0.713	0.599	0.767	(0.566)
Globeland30	PA	0.896	0.698	0.765	0.539	0.455	0.824	0.752	0.643	0.492	0.831	0.777
	UA	0.891	0.906	0.444	0.527	0.157	0.893	0.500	0.703	0.829	0.705	(0.437)
FROM_GLC	PA	0.485	0.714	0.640	0.254	0.032	0.904	0.760	0.506	0.681	0.501	0.591
	UA	0.872	0.809	0.193	0.139	0.186	0.884	0.696	0.808	0.496	0.703	(0.360)
GLC_FCS30	PA	0.865	0.779	0.398	0.565	0.363	0.869	0.051	0.648	0.658	0.742	0.748
	UA	0.857	0.832	0.509	0.330	0.132	0.942	0.573	0.643	0.462	0.752	(0.418)

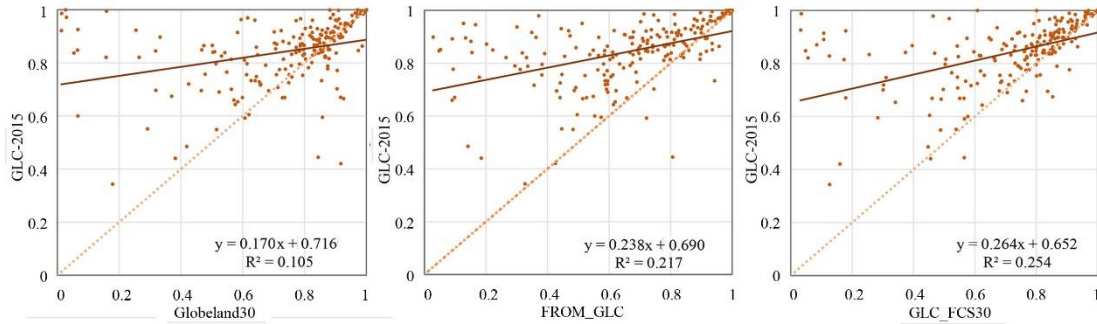
550 Accuracy assessment was calculated in each patch-based sample, and box plots were produced for
 551 each GLC product at the continental scale, as shown in Figure 8. The GLC-2015 map showed a robust
 552 performance in each continent, with the highest OA and kappa coefficient among all the maps. Also, in
 553 all continents, the GLC-2015 map had the shortest boxes in terms of OA, which denoted that it had a

554 more minor variation in accuracy at the continental scale. Among four products, the GLC_FCS30 and
 555 Globeland30 achieved similar accuracies in most continents. Obviously, the FROM_GLC showed lowest
 556 accuracy across different continents, especially in Oceania, where the OA of most patch-based samples
 557 was below 40.0%, namely most of the pixels in Oceania were incorrectly classified. We further compared
 558 mapping accuracies for each LC class in different continents (Figures S3-S4). Since tundra and
 559 permanent snow and ice are rare and only existent in certain regions, they were not included in the
 560 comparison. As for PA across different continents, the GLC-2015 map outperformed other maps in forest,
 561 water bodies, and bare land. As for UA across different continents, the GLC-2015 map outperformed
 562 other maps in cropland, grassland, shrubland and wetland, and achieved similar accuracies with the
 563 GLC_FCS30 and Globeland30 in forest. Overall, the GLC-2015 map outperformed others regarding
 564 mapping accuracy at continental scale. In addition, all GLC products showed significant variation and
 565 low mean accuracy in grassland, shrubland, and wetland over most continents.



566
 567 **Figure 8. The box-plot of the accuracy for different continents. (a) overall accuracy, (b) kappa coefficient.**

568 Furthermore, to compare the OA of the GLC-2015 map with other GLC products, scatter plots were
 569 used to describe the relationship between the overall accuracy of the GLC-2015 map and one other
 570 product in each patch-based sample, as displayed in Figure 9. Most of the points were above the 1:1 line,
 571 implying that the GLC-2015 map surpassed other GLC products in terms of OA. The distribution of
 572 points was more dispersed from the 1:1 line in the plot of the GLC-2015 map against FROM_GLC
 573 compared to other plots. It indicated that these two products had a more significant difference, which
 574 was also proved in Table 6.



575

576

Figure 9. Scatter plots between the GLC-2015 map and other products obtained using the global patch-based samples.

577

578

4.3.3 Areal comparison for individual classes

579

To assess the similarities and discrepancies between the GLC-2015 and other GLC products, we compared the area of various LC classes at multiple scales, including global, continental, national, and ecoregional scales.

580

581

582

The areal comparison for various classes of different GLC products over the globe is shown in Figure 10. Generally, the areas of water bodies and permanent snow and ice of four GLC products were very similar, which may be related to the similar LC definitions. In contrast, the areas of cropland, forest, grassland, and shrubland in GLC-2015 differed significantly from those in other GLC products. The area of forest in GLC-2015 is much higher than other products. This may be because FROM_GLC and GLC_FCS30 defined forest with tree cover over 15%, while GLC-2015 used a threshold of over 10%. The cropland areas in GLC-2015 and Globeland30 were close, higher than FROM_GLC but lower than GLC_FCS30. Moreover, the FROM_GLC underestimated the cropland area as it had a low producer's accuracy for cropland (see Table 5), which was also demonstrated in previous researches (Liu and Xu, 2021; Zhang et al., 2021). FROM_GLC and Globeland30 shared similar grassland areas since a similar accuracy for grassland was found in these two products (see Table 5). However, the FROM_GLC and Globeland30 significantly overestimated grassland extent, with much bare land misclassified as grassland (Hu et al., 2014). The GLC_FCS30 showed the smallest area for grassland, which might be related to its higher threshold in vegetation cover for grassland. For shrubland, the area difference between GLC-2015 and Globeland30 was minimal, and the areas in FROM_GLC and GLC_FCS30 were similar. Furthermore, the wetland area in FROM_GLC was the lowest among all the products, with a total area of 0.168 million km². In contrast, the Globeland30 and GLC_FCS30 exhibited greater wetland extent than GLC-2015 since these two products classified non-wetlands sensitive to water as wetlands

583

584

585

586

587

588

589

590

591

592

593

594

595

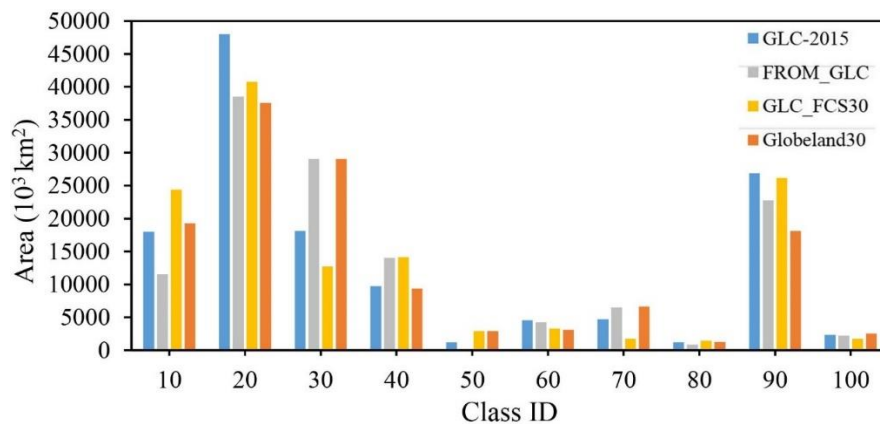
596

597

598

599

600 (Zhang et al., 2023). In particular, the tundra area in GLC_FCS30 was much smaller than other products.
 601 This is mainly because only lichens/mosses in the original classification system of GLC_FCS30 was
 602 converted into tundra in the classification system we used, which leads to the omission of tundra. The
 603 areas of impervious surfaces in GLC-2015, Globeland30, and GLC_FCS30 were very close and higher
 604 than FROM_GLC. For bare land, there was large difference between Globeland30 and other products,
 605 while the area in GLC-2015 and GLC_FCS30 was very close.



606
 607 **Figure 10. Areal comparison of various land cover classes among GLC products at the global scale. Class IDs**
 608 **10, 20, 30, 40, 50, 60, 70, 80, 90, and 100 denote cropland, forest, grassland, shrubland, wetland, water bodies,**
 609 **tundra, impervious surfaces, bare land, and permanent snow and sea ice, respectively.**

610 The area similarity and difference for various classes of different GLC products were also compared
 611 over six continents, the top 40 countries ranked by area, and 21 ecoregions (Figures S5-S7). Overall, the
 612 four products showed a similar distribution trend of different classes. For most LC classes, the continental,
 613 national, and ecoregional rankings of four products agreed with their ranking at the global scale. Whereas,
 614 for grassland and shrubland, the area ranking of four products varied at three different regional scales.

615 4.3.4 Visual inter-comparison for individual classes

616 The visual comparison of cropland in GLC-2015, Globeland30, FROM_GLC, GLC_FCS30, [Global](#)
 617 [Food Security-Support Analysis Data \(GSFAD30\)](#) (Xiong et al., 2017; Teluguntla et al., 2018), and other
 618 national-scale maps was conducted in three local regions (Figure S8). In the Egyptian agricultural area,
 619 GLC-2015, FROM_GLC, and GLC-FCS30 shared similar delineation of the cropland and had a good
 620 representation of cropland with fine spatial details. Since the date time of the Google Earth image is 2015,
 621 Globeland30 missed the newly cultivated cropland. GFASD30 had the largest cropland area among five
 622 products but misclassified bare land as cropland. In the agricultural area of Southeastern China, GLC-

623 2015 had an agreement with GFSAD30 and CLCD. Globeland30 and GLC_FCS30 overestimated the
624 area of cropland. As for FROM_GLC, it failed to depict the spatial distribution of cropland and had many
625 omissions. In cropland-dominated areas of the United States, FROM_GLC significantly underestimated
626 the extent of cropland. The other five products exhibited a similar delineation of cropland, but there were
627 little differences in some small areas. For example, Globeland30 misclassified some grassland into
628 cropland, and NLCD 2016 had a good ability to distinguish the farm rack.

629 We also compared the performance in the forest of different products in three forest-prevalent
630 regions of Congo, China, and the United States (Figure S9). Overall, GLC-2015 and Globeland30
631 showed accurate delineation in three regions. FROM_GLC also had good performance for the forest in
632 Congo and USA but overestimated the forest in China, mislabeling shrubland and grassland as forest.
633 Furthermore, GFC tended to miss sparse trees in China, and GLC_FCS30 underestimated the extent of
634 forest in both three regions. As for national-scale products, CLCD and NLCD 2016 had a good ability to
635 identify the details of forest, while CLUD dramatically missed both dense and sparse woodlands.

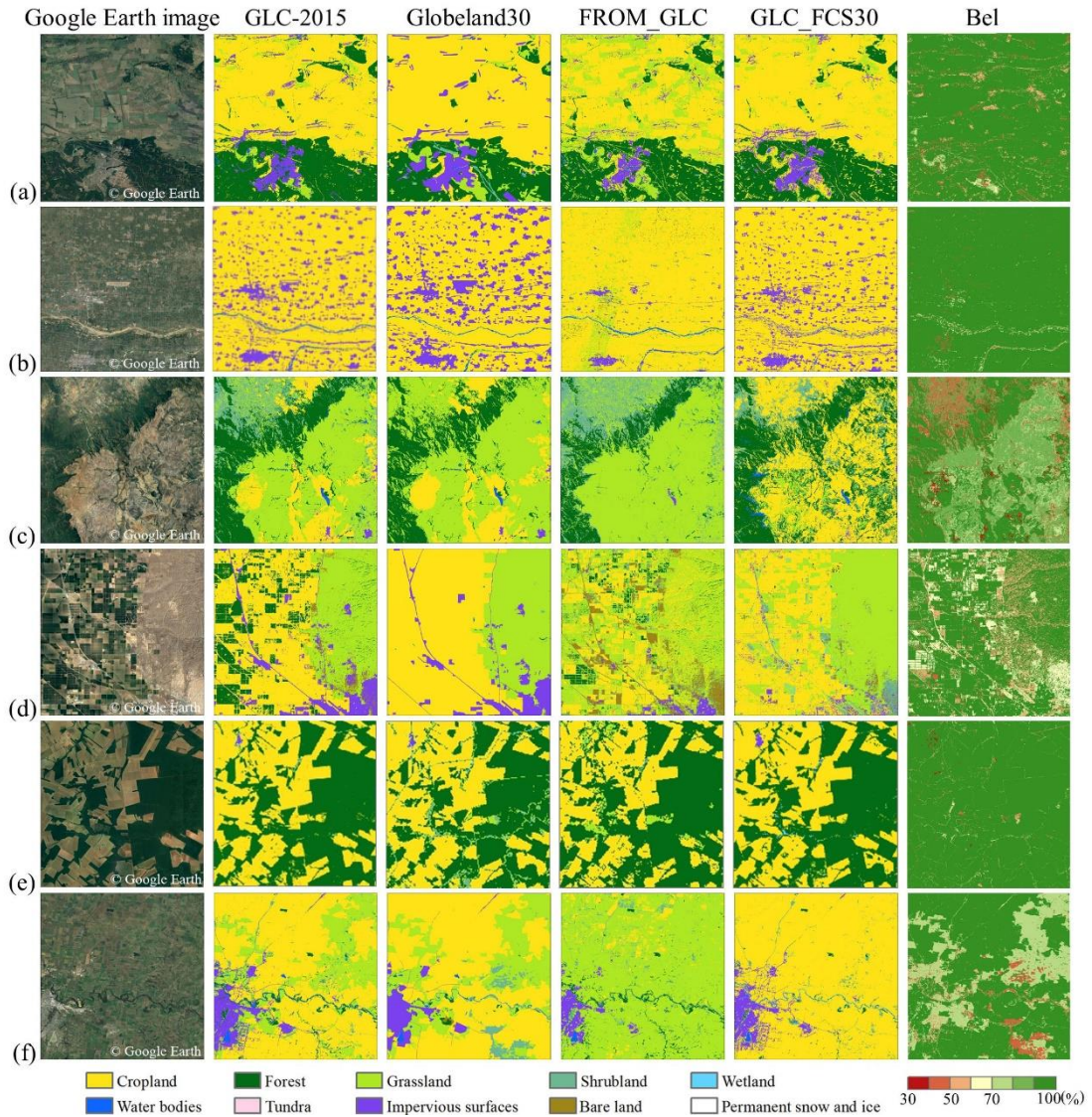
636 Furthermore, to compare the performance in the wetland of GLC-2015 with other global and
637 national-scale products, three wetland regions in South-central Canada, coastal America, and Sundarbans
638 were selected. It can be found that GLC-2015 and Globeland30 had similar representation and performed
639 well in identifying the wetland over three regions (Figure S10). Unexpectedly, FROM_GLC performed
640 poorly in each region, with almost no wetlands captured. GLC_FCS30 also showed unstable quality in
641 three regions. For example, it highly underestimated the wetland area in coastal America and completely
642 mislabeled the mangroves as cropland in Sundarbans. NLCD 2016 and GMW accurately demonstrated
643 the spatial pattern of the wetland, while the CA_wetlands map underestimated the wetland extent because
644 it defined wetlands by wetland frequency of no less than 80% from 2000 to 2016 (Wulder et al., 2018).

645 To understand the spatial distribution of impervious surfaces in different products, a comparison of
646 mapping results for three megacities, including Tokyo, Shanghai, and New York, was shown in Figure
647 S11. In Tokyo, a high consistency was found between GLC-2015, FROM_GLC, and GAUD, and both
648 successfully captured the impervious surfaces in peri-urban areas. GLC_FCS30 showed the largest area
649 for impervious surfaces because it misclassified many croplands into impervious surfaces. In Shanghai,
650 GLC_FCS30 underestimated the central city, and CLUD lost the details of impervious surfaces because
651 it was developed using the visual interpretation method. Other products generally had the similar

652 representation and accurately demonstrated the spatial distribution of the city. For New York, the
653 FROM_GLC, GLC_FCS30, and GAUD agreed well with GLC-2015, while Globeland30 and NLCD
654 2016 had high impervious areas than others.

655 **4.3.5 Visual inter-comparison at the local scale**

656 We selected six typical geographical tiles covering six continents and different landscape environments
657 to further present the mapping performance of the GLC-2015 map, Globeland30, FROM_GLC, and
658 GLC_FCS30, as shown in Figure 11. Overall, from a local point of view, the GLC-2015 map tended to
659 be more diverse in LC classes and had better identification performance in various classes. In flattened
660 cropland areas (Figure 11a and Figure 11b), the GLC-2015 map revealed diverse LC classes and
661 accurately distinguished impervious surfaces; however, the Globeland30 exaggerated the extent of
662 impervious surfaces, and the FROM_GLC failed to delineate impervious surfaces with small size. In
663 addition, the FROM_GLC misclassified some cropland pixels as grassland (Figure 11a) and had an
664 abnormal “stamp” (Figure 11b). As for mountain areas (Figure 11c and Figure 11d), the GLC-2015 map
665 uncovered the spatial pattern of natural and planted forest, cropland, and grassland. There were large
666 confusions between cropland and grassland in the results of the FROM_GLC and GLC_FCS30, and
667 some impervious surfaces and cropland areas were wrongly labeled as bare land by the FROM_GLC.
668 The areas (Figure 11c), which were classified as forest, were misidentified as cropland and grassland in
669 three other products. For the rainforest areas where a large number of trees were reclaimed for cropland
670 (Figure 11e), the GLC-2015 map, Globeland30, and GLC_FCS30 had similarities in cropland areas; but
671 the FROM_GLC recognized some reclaimed areas as grassland. Additionally, the GLC-2015 map
672 accurately presented the spatial distribution of impervious surfaces while other products had omission or
673 commission errors. In the cropland-dominated areas (Figure 11f), the GLC-2015 map and Globeland30
674 showed a higher agreement, and both of them mapped the undulating areas as grassland. Unlike the
675 aforementioned two products, the FROM_GLC misclassified large tracts of croplands as grasslands, and
676 the GLC_FCS30 did not capture the grassland in undulating areas. Figure 11 also shows the belief
677 measure of the fused result in different geographical tiles. Although it does not directly evaluate the
678 mapping accuracy, it serves as a degree of support for the hypothesis of an accepted LC class being true,
679 it can still reflect the quality of the GLC-2015 map. Overall, Bel of the GLC-2015 map exceeded 80%
680 in most areas of each tile, demonstrating the credibility and high quality of our mapping result.



681

682 **Figure 11. Visual comparison between the GLC-2015 map and three other products for different continents.**
 683 **(a) to (f) are examples for Europe, Asia, Africa, North America, South America, and Oceania, respectively.**

684 **4.4 Inter-comparison with national-scale products**

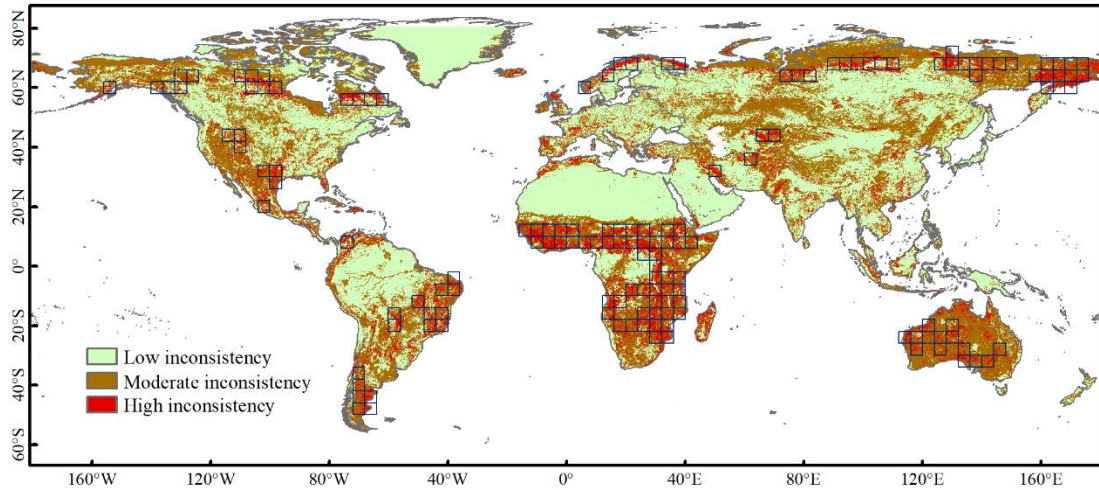
685 Except for comparison with the existing GLC products, the GLC-2015 was also compared with
 686 three national-scale products (CLCD, CLUD, and NLCD 2016 over CONUS). We first compared the
 687 accuracy of the GLC-2015 with NLCD, CLCD, and CLUD using the point-based samples (Tables S5-
 688 S6). It can be found that the GLC-2015 obtained an overall accuracy of 88.8% in China, higher than
 689 CLCD (78.3%) and CLUD (70.2%). Specifically, the GLC-2015 achieved the highest PA and UA in all
 690 LC classes except wetland. In the CONUS, the GLC-2015 outperformed NLCD 2016 with an OA
 691 improvement of 13.2%. Additionally, the GLC-2015 exhibited better mapping performance in nearly all
 692 LC classes.

693 An accuracy comparison between the GLC-2015 and three national-scale products was also
694 performed using the patch-based samples (Tables S7-S8). Overall, the GLC-2015 achieved a better OA
695 of 85.7% in China, with respect to CLCD (83.6%) and CLUD (75.4%). In terms of PA and UA, the GLC-
696 2015 ranked first or second in most LC classes. In the CONUS, the GLC-2015 possessed an OA of 84.5%
697 and a kappa coefficient of 0.787, outperforming NLCD 2016. Although the GLC-2015 had lower PAs in
698 wetland and impervious surfaces, and lower UAs in cropland and forest compared to NLCD 2016, the
699 GLC-2015 outperformed NLCD 2016 in most LC classes.

700 We further performed an areal comparison for each LC class of GLC-2015 and three national-scale
701 products (Figures S12-S13). Generally, the GLC-2015, CLCD, and CLUD exhibited similar areas in
702 most classes. Notably, the areas of cropland, shrubland, and wetland in GLC-2015 were very close to
703 CLCD but different from CLUD. In the CONUS, the areas of cropland, water bodies, and bare land in
704 the GLC-2015 and NLCD 2016 were close. In contrast, the areas of the remaining LC classes in the
705 GLC-2015 showed a large difference from NLCD 2016. The area differences in forest, grassland and
706 shrubland between GLC-2015 and NLCD 2016 were mainly related to different LC definitions. For
707 example, the minimum fraction of tree cover in the forest is 10% in GLC-2015, whereas NLCD 2016
708 used a minimum fraction of 20%. NLCD 2016 had higher area of impervious surfaces than the GLC-
709 2015 because open urban in NLCD 2016 includes too much vegetation.

710 **4.5 Improvement of the GLC-2015 map compared to existing GLC products**

711 The spatial distribution of inconsistency between three GLC products at the global scale is illustrated in
712 Figure 12. From the inconsistency map, we found that areas of low inconsistency mainly corresponded
713 to homogeneous regions with simple LC classes. For example, the northern part of Africa was mainly
714 classified as bare land, the northern part of South America was mainly classified as forest, and the
715 Greenland was classified as permanent snow and ice. On the contrary, areas of high inconsistency were
716 located in regions with complicated LC classes, especially in mixed vegetation regions or sparse
717 vegetation regions, such as northern Asia, South Africa, Sahel region, Australia, northern and southern
718 North America, and eastern and southern South America.



719

720 **Figure 12. Distribution of inconsistency between the Globeland30, FROM_GLC, and GLC_FCS30.** The blue
 721 rectangles are high-inconsistency grids that the area of pixels with value equal to 1 account for more than 20%
 722 of the total area.

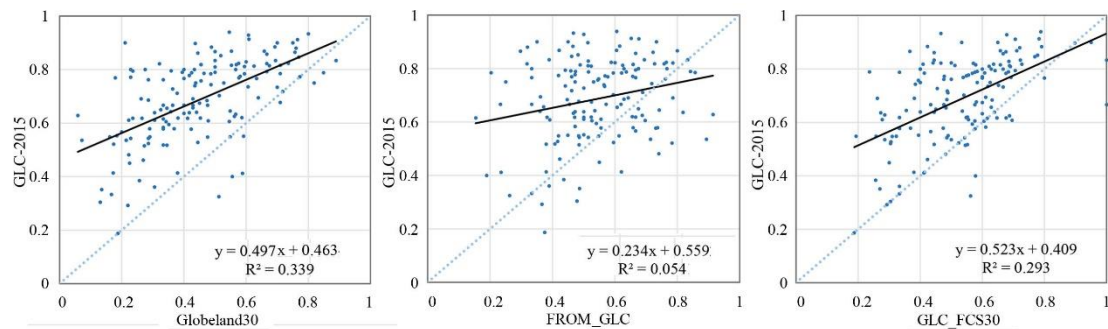
723 Based on the global point-based samples, we assessed the accuracies of the GLC-2015 map,
 724 Globeland30, FROM_GLC, and GLC_FCS30, in the aforementioned areas of low inconsistency,
 725 moderate inconsistency, and high inconsistency, as shown in Table 7. Overall, the GLC-2015 map had
 726 the highest accuracies against the other three ones in three areas. For each product, areas of low
 727 inconsistency obtained the highest accuracies, followed by areas of moderate inconsistency and then high
 728 inconsistency, which demonstrated that inconsistency of the existing products could indicate the quality
 729 of maps. In areas of low inconsistency, the overall accuracy gap between the GLC-2015 map and
 730 previous ones was as small as 0.1%-0.6%. However, for areas of moderate and high inconsistency, the
 731 comparison accuracy gap expanded to 19.3%-28.0% and 27.5%-29.7%, respectively. It proved the
 732 outperformance of the GLC-2015 map over the other three products in the areas of high identification
 733 difficulty.

734 **Table 7. Accuracy assessments of the GLC products in three areas.**

	GLC-2015		Globeland30		FROM_GLC		GLC_FCS30	
	OA	Kappa	OA	Kappa	OA	Kappa	OA	Kappa
Areas of low inconsistency	0.951	0.938	0.945	0.929	0.950	0.936	0.951	0.937
Areas of moderate inconsistency	0.760	0.723	0.561	0.498	0.480	0.411	0.567	0.495
Areas of high inconsistency	0.567	0.498	0.292	0.204	0.286	0.198	0.270	0.160

735 We further provided a comparative analysis of three previous GLC products and the GLC-2015 map

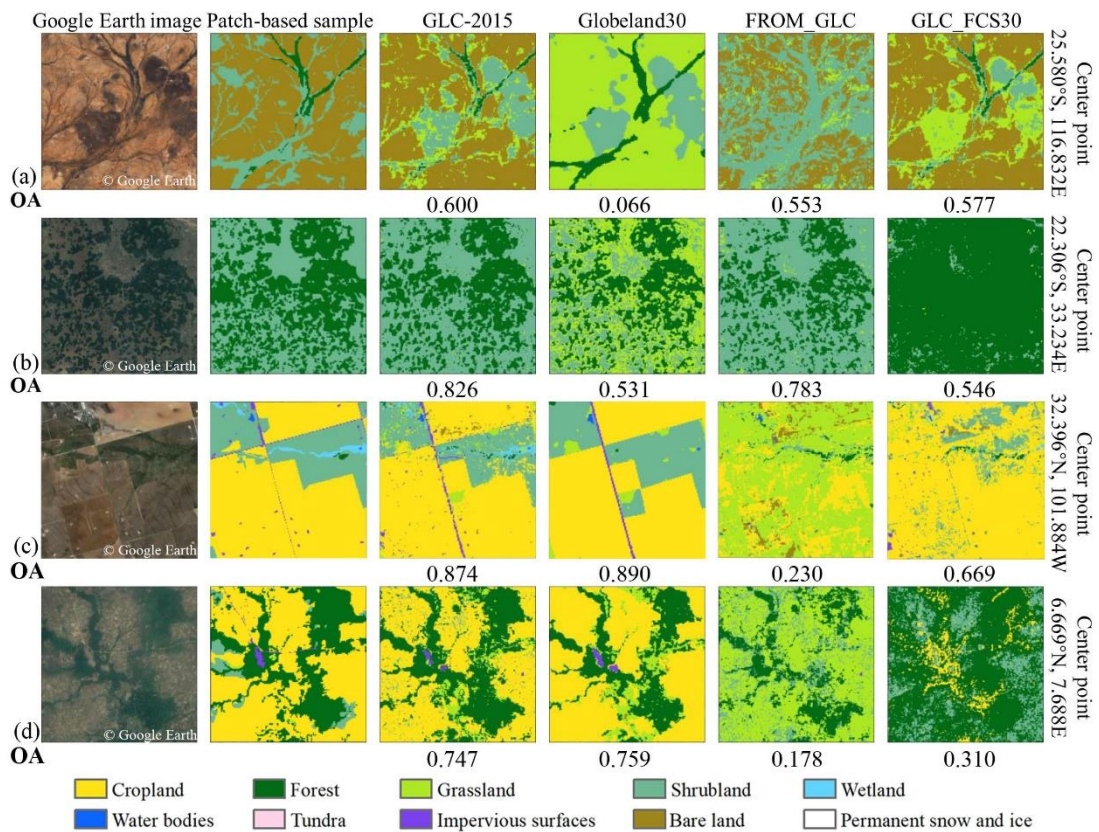
736 in areas of high inconsistency. We calculated the area of pixels with a value equal to 1 in $4^{\circ} \times 4^{\circ}$ grids.
 737 The grids that the area of pixels with a value equal to 1 account for more than 20% of the total area was
 738 selected as grids of high inconsistency. Finally, a total number of 147 grids were selected (Figure 13). To
 739 compare the accuracy of the GLC-2015 map and other ones, we utilized scatter plots to represent the
 740 relationship between the overall accuracy of one previous product and the GLC-2015 map in each grid
 741 of high inconsistency based on the global point-based samples (Figure 13). Most of the points were above
 742 the 1:1line, namely the values of y-axes corresponding to those points were larger than the values of x-
 743 axes, which demonstrated that the GLC-2015 map performed better than other GLC products in most
 744 grids of high inconsistency. It can be found that the fitting line in each scatter plot had the intercept
 745 exceeding 0.40, the slope less than 0.55, and the R^2 less than 0.35, showing that the GLC-2015 map had
 746 a large difference with other ones.



747
 748 **Figure 13. Overall accuracy relationship between the GLC-2015 map and other products in grids of high**
 749 **inconsistency.**

750 To intuitively compare the mapping result of the GLC-2015 map and three existing ones in areas of
 751 high inconsistency, we focused on visual inspection in various areas based on four $5\text{ km} \times 5\text{ km}$ patch-
 752 based samples and conducted accuracy statistics, as shown in Figure 14. In the detailed display, it is
 753 apparent that three previous products had a large difference in four areas. As can be seen from the four
 754 visual cases, the typical confusions between LC classes in areas of high inconsistency were as follows:
 755 (1) shrubland was easily misclassified as forest and grassland; (2) cropland, grassland, and shrubland
 756 were heavily confused with each other; (3) bare land was likely to be mixed with shrubland and grassland.
 757 Overall, the GLC-2015 map surpassed other products in the local accuracy assessment. In Western
 758 Australian mulga shrublands (Figure 14a), the GLC-2015 map and GLC_FCS30 showed similar spatial
 759 distribution and shape of bare land and forest, which was consistent with the real landscape. While the
 760 Globeland30 classified bare land as grassland and the FROM_GLC under-classified bare land. As for

761 Zambebian and mopane woodlands (Figure 14b), the GLC-2015 map performed best with OA reaching
 762 82.6%, followed by the FROM_GLC. In contrast, other products mixed shrubland with forest or
 763 grassland. In agricultural land of Western United States (Figure 14c), the GLC-2015 and Globeland30
 764 exhibited similar mapping results with the ground truth while the FROM_GLC had large difference with
 765 other products. When it comes to Guinean forest-savanna mosaic (Figure 14d), the GLC-2015 map and
 766 Globeland30 showed high spatial consistency, and both had accurate classification profile for cropland,
 767 forest, and impervious surfaces, while other products misidentified cropland as other LC classes.



768
 769 **Figure 14. Visual comparison between the GLC-2015 map and three other products based on 5km × 5km**
 770 **patch-based samples and Google Earth images for four areas of high inconsistency (a-d). The OA for each**
 771 **product was calculated by the corresponding patch-based sample.**

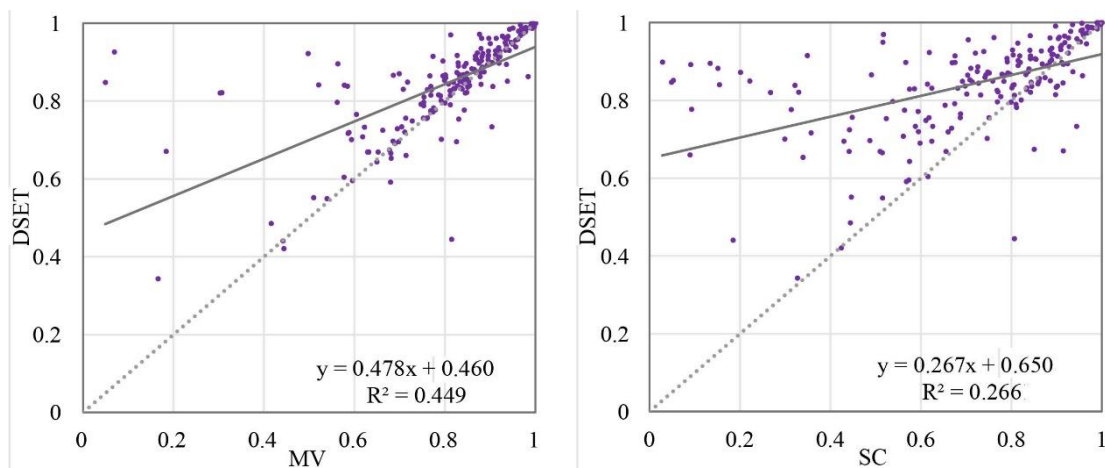
772 **4.6 Comparison between DSET and other methods**

773 **4.6.1 Inter-comparison with other data fusion methods**

774 The accuracy assessments on GLC-2015 obtained by DSET and global mapping results from two other
 775 data fusion methods were conducted based on two global validation sample sets. The confusion matrixes
 776 with the global point-based samples are shown in [Table S9](#) and [S10](#). The OA of the global land cover

777 classification obtained by the MV and SC was 72.1% and 71.8%, respectively. As shown in Table 3, the
778 OA of the GLC-2015 map obtained by the DSET method was 79.5%, which had an improvement of 7.4%
779 and 7.7% compared to mapping results from the MV and SC. In addition, the GLC-2015 map obtained
780 higher PA and UA for most LC classes.

781 When evaluating GLC maps obtained by different data fusion approaches using the global patch-
782 based samples, the DSET method obtained the highest OA of 83.6% and kappa coefficient of 0.566,
783 compared with 80.1% and 0.497 for MV, and 71.8% and 0.391 for SC (Table S11). Here, the DSET
784 method achieved an accuracy improvement of 3.5% and 11.8%. Compared to the two other methods, the
785 DSET improved the accuracy for nearly all the LC classes, especially for grassland, shrubland, and
786 wetland. We also compared the overall accuracy relationship between the DSET and other methods. From
787 the scatter plots (Figure 15), we found that the majority of points were above the 1:1 line, implying DSET
788 had better mapping performance than others in most regions across the globe.



789
790 **Figure 15. Scatter plots between the DSET and other data fusion methods based on the global patch-based**
791 **samples.**

792 Land cover mapping results from the DSET and other methods were also visually illustrated in six
793 tiles with size of the 0.25° covering different continents, as displayed in Figure S14. Despite that mapping
794 results from the DSET and MV depicted similar spatial distribution of LC classes in all tiles except the
795 tile in North America, the DSET more accurately delineated the impervious surfaces of small size which
796 scattered in cropland-dominated (Figure S14a) or arid areas (Figure S14c). Notably, the mapping results
797 from the SC method presented significant differences from that obtained by the DSET and MV. For
798 example, the SC method failed to capture scattered rural residential areas (Figure S14b) and misclassified
799 grassland as cropland (Figure S14d). Overall, the DSET method possessed better recognition

800 performance in various LC classes than the other two methods.

801 **4.6.2 Inter-comparison with the Random Forest**

802 Based on the validation data from 20% of the global point-based samples, we evaluated the quality of
803 the GLC-2015 map obtained by the DSET method and mapping results classified by the RF classifier for
804 a total of 300 grids. The DSET method obtained a mean OA of 80.9% across six continents, while the
805 RF achieved a lower accuracy of 69.9%. From the scatter plots which compared the OA and kappa
806 coefficient between the DSET and RF grid by grid, it was found that the DSET possessed higher accuracy
807 in most grids (Figure S15). Especially, the points were clustered in the upper right corner of the plot
808 (Figure S15a), which indicated that the RF classifier trained with the global point-based samples
809 performed well in those selected grids though it was inferior to the DSET method. Figure S16 shows the
810 OA of the DSET and RF across six continents. We found that the DSET method outperformed RF
811 classifier for each continent. Especially, the mapping results of both two methods presented the lowest
812 accuracy in Oceania. It may be because the selected grids are located in regions with heterogeneous
813 landscape. As for the box plot for the RF classifier, the low hinge exceeded 60.00% in all continents
814 except Oceania, demonstrating the reliability of the RF classifier trained by the global point-based
815 samples. Nevertheless, the performance of the RF classifier was worse than the DSET method. This
816 highlights the feasibility of the DSET method in integrating the existing maps for a better one.

817 **4.7 Advancement and Limitations**

818 To address the problem that current 30m GLC products have great inconsistency in heterogeneous
819 areas and low mapping accuracy for spectral similar LC classes, this study adopted a multi-source
820 product fusion approach based on DSET to create an improved global land cover map (GLC-2015). The
821 results show that the GLC-2015 had good mapping performance with OA reaching 79.5% and 83.6%
822 based on two different validation sets. Compared with those existing products, the GLC-2015 greatly
823 improved the accuracy across the globe, especially in areas of high inconsistency with a significant
824 improvement of 27.5%-29.7%. Compared with other commonly used data fusion methods, the adopted
825 DSET approach provided higher OA and kappa coefficient which showed the benefit of the DEST in
826 integrating various land cover data. No matter from the respective of the global point-based samples or
827 the global patch-based samples, the GLC-2015 showed relatively low accuracy for grassland, shrubland,

828 and wetland compared to other LC classes. Those LC classes are challenging to map at the global scale
829 duo to their spectral similarity to other classes, ambiguous definitions, or variety with regions. However,
830 compared to other existing 30m GLC products, the GLC-2015 map performed better with the PA and OA
831 ranking first or second for grassland, shrubland, and wetland, which indicated the improvement of the
832 GLC-2015 in poorly-mapped LC classes. It was found that the GLC-2015 map had worse performance
833 in areas with more disagreements (Table 7). However, the GLC-2015 map surpassed other products in
834 the areas with different agree of inconsistency. Moreover, the accuracy gap between the GLC-2015 map
835 and other ones in areas of high inconsistency was larger than that in areas with fewer disagreements,
836 implying that the GLC-2015 map provides a more accurate characterization of land cover in poorly-
837 mapped areas. Although the GLC-2015 map was not capable of avoiding all the wrong mapping results
838 caused by the disagreements from the candidate GLC products, it outperformed the existing products
839 from the aspects of mapping accuracy for the easily misclassified classes and areas with great
840 inconsistency.

841 Although the GLC-2015 map can evidently improve mapping accuracy in inconsistent areas, there
842 are still some uncertainties. First, we used three multiple-class GLC maps and four single-class GLC
843 maps as the source data for integration. Since those products provided information of land cover at the
844 global scale, classification errors inevitably exist in some specific regions. The multisource product
845 fusion method based on DEST depends highly on the quality of those candidate maps such that the
846 inconsistency between those source maps might lead to incorrect classification. Second, the date time of
847 the GlobeLand30 is different from that of other maps. Because of the five-year time interval, there are
848 changes in land cover, which inevitably distort the fusion results. However, the changed areas are tiny
849 compared to the world's terrestrial area. The uncertainties caused by the LC changes are minor than those
850 from classification errors. In addition, the global point-based samples were used to evaluate the reliability
851 of each product. The accuracy of GlobeLand30 was lower than the other products for areas with LC
852 changes. In this case, the fusion depended more on other maps to avoid the errors caused by LC changes.
853 Third, due to the different LC definitions, uncertainties in classification system conversion are inevitable
854 (Zhang et al., 2017), which might cause problems for the fusion based on the DSET method. However,
855 we conducted a reliability evaluation of the candidate maps to reduce the influence of uncertainties in
856 classification system conversion on the fusion. The point-based samples used for reliability evaluation

857 were labeled referring to the LC definitions in our classification system so that all the maps were
858 evaluated under the criterion of the classification system we used. By the reliability evaluation, the
859 candidate maps were assessed to have lower accuracy for areas with mismatched information. When
860 integrating all the maps grid by grid, the mismatched information would contribute less to the fusion.
861 Lastly, most candidate LC products used a simple classification system without a level-2 classification
862 system, so they made no contributions to a more detailed classification system when they served as source
863 data for data fusion. Although some maps provided detailed LC classification results, such as the
864 GLC_FCS30 and FROM_GLC for 2015, there might be several challenges in the standardization and
865 uniformity of level-2 classification systems due to the large discrepancies in the definition and criteria.
866 Therefore, the GLC-2015 adopted a simple classification system containing 10 major LC classes. In
867 future work, measures will be taken to meet the expectation of a more detailed classification system for
868 GLC mapping. An improved GLC product with a detailed classification system rather than a simple one-
869 level classification system can be further developed based on the highly applicable and general DSET
870 method whenever more products with diverse LC classes are available. Additionally, a feasible
871 framework for the conversion of different level-2 classification systems into a uniform system should be
872 developed.

873 **5. Data availability**

874 The improved global land cover map in 2015 with 30 m resolution is available at
875 <https://doi.org/10.6084/m9.figshare.22358143.v2> (Li et al., 2022). The GLC-2015 product is organized
876 by a total of $1507\ 4^{\circ} \times 4^{\circ}$ geographical grids in GeoTIFF format across the world's terrestrial area. Each
877 image of the GLC-2015 product is named as "GLC-2015_lon_lat" (lon and lat represent the longitude
878 and latitude and of the grid's lower left corner, respectively).

879 **6. Conclusions**

880 GLC information at fine spatial resolution is vital for the global environment and climate studies which
881 can capture the footprint of human activity. Resulting from the differences in classification scheme,
882 satellite sensor data, classification algorithms and sampling strategies, the existing GLC products have
883 high inconsistency in some parts of the world, especially in fragmented areas and transition zones. More

884 accurate and reliable data with accuracy improved in areas of high mapping inconsistency is very
885 desirable. In this study, with the help of the GEE platform, we developed the GLC-2015 map by
886 integrating multiple existing GLC maps based on the DSET. The GLC-2015 map can significantly
887 increase the mapping accuracy and possess good recognition performance in various LC classes.

888 The GLC-2015 map was validated by both the global point-based samples and the global patch-
889 based samples. Accuracy assessments show that the GLC-2015 map achieved an OA of 79.5%, a kappa
890 coefficient of 0.757 using a total of 34,117 global point-based samples, and an OA of 83.6%, a kappa
891 coefficient of 0.566 using a total of 201 global patch-based samples. Data inter-comparison indicated
892 that the GLC-2015 map surpassed other three products both visually and quantitatively, by OA
893 improvement of 14.0%-17.8% validated with the global point-based samples and 5.9%-24.5% with the
894 global patch-based samples. Compared to other products, there are fewer misclassifications in the GLC-
895 2015 map for most LC classes, such as forest, cropland, shrubland, and water bodies. Meanwhile, the
896 GLC-2015 map outperformed others in terms of OA and kappa coefficient across different ecoregions
897 and different continents. Notably, the GLC-2015 map showed better performance than others by an
898 increment of 0.1%-0.6% in overall accuracy for areas of low inconsistency, 19.3%-28.0% for areas of
899 moderate inconsistency, and 27.5%-29.7% for areas of high inconsistency. In addition, the mapping
900 results obtained by the DSET surpassed other data fusion methods with OA improvement of 7.4%-7.7%
901 via the global point-based samples and 3.5%-11.8% via the global patch-based samples. Therefore, it can
902 be concluded that the GLC-2015 map is a robust and reliable map that can significantly improve mapping
903 accuracy compared to previous GLC products and mapping results from other common data fusion
904 methods.

905 **Author contributions**

906 XL and XX conceived the research. BL and XX designed and carried out the experiments. QS and DH
907 provided data. BL wrote the original manuscript. XX, HZ and YC reviewed the writing.

908 **Competing interests**

909 The authors declare that they have no conflict of interest.

910 **Financial support**

911 This research has been supported by the National Key Research & Development Program of China (Grant
912 No. 2019YFA0607203), the National Natural Science Foundation of China (Grant No. 42001326,
913 42171409), and the Natural Science Foundation of Guangdong Province of China (Grant No.
914 2022A1515012207).

915 **References**

- 916 Ban, Y., Gong, P., and Giri, C.: Global land cover mapping using Earth observation satellite data: Recent
917 progresses and challenges, *ISPRS J. Photogramm.*, 103, 1-6,
918 <https://doi.org/10.1016/j.isprsjprs.2015.01.001>, 2015.
- 919 Bartholomé, E. and Belward, A. S.: GLC2000: A new approach to global land cover mapping from Earth
920 observation data, *Int. J. Remote Sens.*, 26, 1959-1977,
921 <https://doi.org/10.1080/01431160412331291297>, 2005.
- 922 Bounoua, L., DeFries, R., Collatz, G. J., Sellers, P., and Khan, H.: Effects of land cover conversion on
923 surface climate, *Clim. Change*, 52, 29-64, <https://doi.org/10.1023/A:1013051420309>, 2002.
- 924 Bunting, P., Rosenqvist, A., Lucas, R. M., Rebelo, L. M., Hilarides, L., Thomas, N., Hardy, A., Itoh, T.,
925 Shimada, M., and Finlayson, C. M.: The Global Mangrove Watch—A new 2010 global baseline of
926 mangrove extent, *Remote Sensing*, 10, <https://doi.org/10.3390/rs10101669>, 2018.
- 927 Chapin, F. S. I., Zavaleta, E. S., Eviner, V. T., Naylor, R. L., Vitousek, P. M., Reynolds, H. L., Hooper,
928 D. U., Lavorel, S., Sala, O. E., Hobbie, S. E., Mack, M. C., and Díaz, S.: Consequences of changing
929 biodiversity, *Nature*, 405, 234-242, <https://doi.org/10.1038/35012241>, 2000.
- 930 Chen, J., Chen, J., Liao, A., Cao, X., Chen, L., Chen, X., He, C., Han, G., Peng, S., Lu, M., Zhang, W.,
931 Tong, X., and Mills, J.: Global land cover mapping at 30m resolution: A POK-based operational
932 approach, *ISPRS J. Photogramm.*, 103, 7-27, <https://doi.org/10.1016/j.isprsjprs.2014.09.002>, 2015.
- 933 Chen, T. M. and Venkataramanan, V.: Dempster-Shafer theory for intrusion detection in ad hoc networks,
934 *IEEE Internet comput.*, 9, 35-41, <https://doi.org/10.1109/MIC.2005.123>, 2005.
- 935 Clinton, N., Yu, L., and Gong, P.: Geographic stacking: Decision fusion to increase global land cover
936 map accuracy, *ISPRS J. Photogramm.*, 103, 57-65, <https://doi.org/10.1016/j.isprsjprs.2015.02.010>,
937 2015.
- 938 Land Cover CCI: Product User Guide Version 2: https://www.esa-landcover-cci.org/?q=webfm_send/84,
939 last access: 21 January 2022.
- 940 DeFries, R. S., Houghton, R. A., Hansen, M. C., Field, C. B., Skole, D., and Townshend, J.: Carbon
941 emissions from tropical deforestation and regrowth based on satellite observations for the 1980s and
942 1990s, *Proc. Natl. Acad. Sci. U.S.A.*, 99, 14256, <https://doi.org/10.1073/pnas.182560099>, 2002.
- 943 Foley, J. A., DeFries, R., Asner, G. P., Barford, C., Bonan, G., Carpenter, S. R., Chapin, F. S., Coe, M. T.,
944 Daily, G. C., Gibbs, H. K., Helkowski, J. H., Holloway, T., Howard, E. A., Kucharik, C. J., Monfreda,
945 C., Patz, J. A., Prentice, I. C., Ramankutty, N., and Snyder, P. K.: Global Consequences of Land Use,
946 *Science*, 309, 570-574, <https://doi.org/10.1126/science.1111772>, 2005.
- 947 Friedl, M. A., Sulla-Menashe, D., Tan, B., Schneider, A., Ramankutty, N., Sibley, A., and Huang, X.:
948 MODIS Collection 5 global land cover: Algorithm refinements and characterization of new datasets,

949 Remote Sens. Environ., 114, 168-182, <https://doi.org/10.1016/j.rse.2009.08.016>, 2010.

950 Fritz, S., You, L., Bun, A., See, L., McCallum, I., Schill, C., Perger, C., Liu, J., Hansen, M., and
951 Obersteiner, M.: Cropland for sub-Saharan Africa: A synergistic approach using five land cover data
952 sets, *Geophys. Res. Lett.*, 38, L04404, <https://doi.org/10.1029/2010GL046213>, 2011.

953 Gao, Y., Liu, L., Zhang, X., Chen, X., Mi, J., and Xie, S.: Consistency analysis and accuracy assessment
954 of three global 30 m land-cover products over the European Union using the LUCAS dataset, *Remote
955 Sensing*, 12, 3479, <https://doi.org/10.3390/rs12213479>, 2020.

956 Gengler, S. and Bogaert, P.: Combining land cover products using a minimum divergence and a Bayesian
957 data fusion approach, *Int. J. Geogr. Inf. Sci.*, 32, 806-826,
958 <https://doi.org/10.1080/13658816.2017.1413577>, 2018.

959 Giri, C., Zhu, Z., and Reed, B.: A comparative analysis of the Global Land Cover 2000 and MODIS land
960 cover datasets, *Remote Sens. Environ.*, 94, 123-132, <https://doi.org/10.1016/j.rse.2004.09.005>, 2005.

961 Giri, C., Pengra, B., Long, J., and Loveland, T. R.: Next generation of global land cover characterization,
962 mapping, and monitoring, *Int. J. Appl. Earth Observ.*, 25, 30-37,
963 <https://doi.org/10.1016/j.jag.2013.03.005>, 2013.

964 Gómez, C., White, J. C., and Wulder, M. A.: Optical remotely sensed time series data for land cover
965 classification: A review, *ISPRS J. Photogramm.*, 116, 55-72,
966 <https://doi.org/10.1016/j.isprsjprs.2016.03.008>, 2016.

967 Gong, P.: Remote sensing of environmental change over China: A review, *Sci. Bull.*, 57, 2793-2801,
968 <https://doi.org/10.1007/s11434-012-5268-y>, 2012.

969 Gong, P., Yu, L., Li, C., Wang, J., Liang, L., Li, X., Ji, L., Bai, Y., Cheng, Y., and Zhu, Z.: A new research
970 paradigm for global land cover mapping, *Ann. GIS*, 22, 87-102,
971 <https://doi.org/10.1080/19475683.2016.1164247>, 2016.

972 Gong, P., Li, X., Wang, J., Bai, Y., Chen, B., Hu, T., Liu, X., Xu, B., Yang, J., Zhang, W., and Zhou, Y.:
973 Annual maps of global artificial impervious area (GAIA) between 1985 and 2018, *Remote Sens.
974 Environ.*, 236, 111510, <https://doi.org/10.1016/j.rse.2019.111510>, 2020.

975 Gong, P., Wang, J., Yu, L., Zhao, Y., Zhao, Y., Liang, L., Niu, Z., Huang, X., Fu, H., Liu, S., Li, C., Li,
976 X., Fu, W., Liu, C., Xu, Y., Wang, X., Cheng, Q., Hu, L., Yao, W., Zhang, H., Zhu, P., Zhao, Z., Zhang,
977 H., Zheng, Y., Ji, L., Zhang, Y., Chen, H., Yan, A., Guo, J., Yu, L., Wang, L., Liu, X., Shi, T., Zhu, M.,
978 Chen, Y., Yang, G., Tang, P., Xu, B., Giri, C., Clinton, N., Zhu, Z., Chen, J., and Chen, J.: Finer
979 resolution observation and monitoring of global land cover: first mapping results with Landsat TM
980 and ETM+ data, *Int. J. Remote Sens.*, 34, 2607-2654, <https://doi.org/10.1080/01431161.2012.748992>,
981 2013.

982 Grekousis, G., Mountrakis, G., and Kavouras, M.: An overview of 21 global and 43 regional land-cover
983 mapping products, *Int. J. Remote Sens.*, 36, 5309-5335,
984 <https://doi.org/10.1080/01431161.2015.1093195>, 2015.

985 Grimm, N. B., Faeth, S. H., Golubiewski, N. E., Redman, C. L., Wu, J., Bai, X., and Briggs, J. M.: Global
986 change and the ecology of cities, *Science*, 319, 756-760, <https://doi.org/10.1126/science.1150195>,
987 2008.

988 Hansen, M. C., Defries, R. S., Townshend, J. R. G., and Sohlberg, R.: Global land cover classification at
989 1 km spatial resolution using a classification tree approach, *Int. J. Remote Sens.*, 21, 1331-1364,
990 <https://doi.org/10.1080/014311600210209>, 2000.

991 Hansen, M. C., Potapov, P. V., Moore, R., Hancher, M., Turubanova, S. A., Tyukavina, A., Thau, D.,
992 Stehman, S. V., Goetz, S. J., Loveland, T. R., Kommareddy, A., Egorov, A., Chini, L., Justice, C. O.,

993 and Townshend, J. R. G.: High-resolution global maps of 21st-century forest cover change, *Science*,
994 342, 850-853, <https://doi.org/10.1126/science.1244693>, 2013.

995 Herold, M., Mayaux, P., Woodcock, C. E., Baccini, A., and Schmullius, C.: Some challenges in global
996 land cover mapping: An assessment of agreement and accuracy in existing 1 km datasets, *Remote Sens.*
997 *Environ.*, 112, 2538-2556, <https://doi.org/10.1016/j.rse.2007.11.013>, 2008.

998 Hu, L., Chen, Y., Xu, Y., Zhao, Y., Yu, L., Wang, J., and Gong, P.: A 30 meter land cover mapping of
999 China with an efficient clustering algorithm CBEST, *Science China Earth Sciences*, 57, 2293-2304,
1000 <https://doi.org/10.1007/s11430-014-4917-1>, 2014.

1001 Hu, S., Niu, Z., Chen, Y., Li, L., and Zhang, H.: Global wetlands: Potential distribution, wetland loss,
1002 and status, *Sci. Total Environ.*, 586, 319-327, <https://doi.org/10.1016/j.scitotenv.2017.02.001>, 2017.

1003 Huang, X., Yang, J., Wang, W., and Liu, Z.: Mapping 10 m global impervious surface area (GISA-10m)
1004 using multi-source geospatial data, *Earth Syst. Sci. Data*, 14, 3649-3672,
1005 <https://essd.copernicus.org/articles/14/3649/2022/>, 2022.

1006 Huang, X., Li, J., Yang, J., Zhang, Z., Li, D., and Liu, X.: 30 m global impervious surface area dynamics
1007 and urban expansion pattern observed by Landsat satellites: From 1972 to 2019, *Science China Earth*
1008 *Sciences*, 64, 1922-1933, <https://10.1007/s11430-020-9797-9>, 2021.

1009 Iwao, K., Nasahara, K. N., Kinoshita, T., Yamagata, Y., Patton, D., and Tsuchida, S.: Creation of new
1010 global land cover map with map integration, *J. Geogr. Inf. Syst.*, 3, 160-165,
1011 <https://doi.org/10.4236/jgis.2011.32013>, 2011.

1012 Jin, Q., Xu, E., and Zhang, X.: A fusion method for multisource land cover products based on superpixels
1013 and statistical extraction for enhancing resolution and improving accuracy, *Remote Sensing*, 14, 1676,
1014 <https://doi.org/10.3390/rs14071676>, 2022.

1015 Jung, M., Henkel, K., Herold, M., and Churkina, G.: Exploiting synergies of global land cover products
1016 for carbon cycle modeling, *Remote Sens. Environ.*, 101, 534-553,
1017 <https://doi.org/10.1016/j.rse.2006.01.020>, 2006.

1018 Kang, J., Wang, Z., Sui, L., Yang, X., Ma, Y., and Wang, J.: Consistency analysis of remote sensing land
1019 cover products in the tropical rainforest climate region: A case study of Indonesia, *Remote Sensing*,
1020 12, 1410, <https://doi.org/10.3390/rs12091410>, 2020.

1021 Kim, D., Lim, C.-H., Song, C., Lee, W.-K., Piao, D., Heo, S., and Jeon, S.: Estimation of future carbon
1022 budget with climate change and reforestation scenario in North Korea, *Adv. Space Res.*, 58, 1002-
1023 1016, <https://doi.org/10.1016/j.asr.2016.05.049>, 2016.

1024 Li, B., Xu, X., Liu, X., Shi, Q., Zhuang, H., Cai, Y., and He, D.: An improved global land cover mapping
1025 in 2015 with 30 m resolution (GLC-2015) based on a multi-source product fusion approach. [dataset],
1026 <https://doi.org/10.6084/m9.figshare.22358143.v2>, 2022.

1027 Li, C., Gong, P., Wang, J., Zhu, Z., Biging, G. S., Yuan, C., Hu, T., Zhang, H., Wang, Q., Li, X., Liu, X.,
1028 Xu, Y., Guo, J., Liu, C., Hackman, K. O., Zhang, M., Cheng, Y., Yu, L., Yang, J., Huang, H., and
1029 Clinton, N.: The first all-season sample set for mapping global land cover with Landsat-8 data, *Sci.*
1030 *Bull.*, 62, 508-515, <https://doi.org/10.1016/j.scib.2017.03.011>, 2017.

1031 Liao, A., Chen, L., Chen, J., He, C., Cao, X., Chen, J., Peng, S., Sun, F., and Gong, P.: High-resolution
1032 remote sensing mapping of global land water, *Science China Earth Sciences*, 57, 2305-2316,
1033 <https://doi.org/10.1007/s11430-014-4918-0>, 2014.

1034 Liu, H., Gong, P., Wang, J., Clinton, N., Bai, Y., and Liang, S.: Annual dynamics of global land cover
1035 and its long-term changes from 1982 to 2015, *Earth Syst. Sci. Data*, 12, 1217-1243,
1036 <https://doi.org/10.5194/essd-12-1217-2020>, 2020a.

1037 Liu, H., Gong, P., Wang, J., Wang, X., Ning, G., and Xu, B.: Production of global daily seamless data
1038 cubes and quantification of global land cover change from 1985 to 2020 - iMap World 1.0, Remote
1039 Sens. Environ., 258, 112364, <https://doi.org/10.1016/j.rse.2021.112364>, 2021a.

1040 Liu, J., Kuang, W., Zhang, Z., Xu, X., Qin, Y., Ning, J., Zhou, W., Zhang, S., Li, R., Yan, C., Wu, S., Shi,
1041 X., Jiang, N., Yu, D., Pan, X., and Chi, W.: Spatiotemporal characteristics, patterns and causes of land
1042 use changes in China since the late 1980s, Dili Xuebao/Acta Geogr. Sin., 69, 3-14,
1043 <https://doi.org/10.11821/dlxb201401001>, 2014.

1044 Liu, K. and Xu, E.: Fusion and correction of multi-source land cover products based on spatial detection
1045 and uncertainty reasoning methods in Central Asia, Remote Sensing, 13, 244,
1046 <https://doi.org/10.3390/rs13020244>, 2021.

1047 Liu, L., Zhang, X., Gao, Y., Chen, X., Shuai, X., and Mi, J.: Finer-resolution mapping of global land
1048 cover: Recent developments, consistency analysis, and prospects, Journal of Remote Sensing, 2021,
1049 5289697, <https://doi.org/10.34133/2021/5289697>, 2021b.

1050 Liu, X., Huang, Y., Xu, X., Li, X., Li, X., Ciais, P., Lin, P., Gong, K., Ziegler, A. D., and Chen, A.: High-
1051 spatiotemporal-resolution mapping of global urban change from 1985 to 2015, Nature Sustainability,
1052 3, 564-570, 2020b.

1053 Liu, X., Huang, Y., Xu, X., Li, X., Li, X., Ciais, P., Lin, P., Gong, K., Ziegler, A. D., Chen, A., Gong, P.,
1054 Chen, J., Hu, G., Chen, Y., Wang, S., Wu, Q., Huang, K., Estes, L., and Zeng, Z.: High-spatiotemporal-
1055 resolution mapping of global urban change from 1985 to 2015, Nature Sustainability, 3, 564-570,
1056 <https://doi.org/10.1038/s41893-020-0521-x>, 2020c.

1057 Loveland, T. R., Reed, B. C., Brown, J. F., Ohlen, D. O., Zhu, Z., Yang, L., and Merchant, J. W.:
1058 Development of a global land cover characteristics database and IGBP DISCover from 1 km AVHRR
1059 data, Int. J. Remote Sens., 21, 1303-1330, <https://doi.org/10.1080/014311600210191>, 2000.

1060 Lu, M., Wu, W., You, L., See, L., Fritz, S., Yu, Q., Wei, Y., Chen, D., Yang, P., and Xue, B.: A cultivated
1061 planet in 2010 – Part 1: The global synergy cropland map, Earth Syst. Sci. Data, 12, 1913-1928,
1062 <https://essd.copernicus.org/articles/12/1913/2020/>, 2020.

1063 Ludwig, C., Walli, A., Schleicher, C., Weichselbaum, J., and Riffler, M.: A highly automated algorithm
1064 for wetland detection using multi-temporal optical satellite data, Remote Sens. Environ., 224, 333-351,
1065 <https://doi.org/10.1016/j.rse.2019.01.017>, 2019.

1066 Mayaux, P., Bartholomé, E., Fritz, S., and Belward, A.: A new land-cover map of Africa for the year 2000,
1067 J. Biogeogr., 31, 861-877, <https://doi.org/10.1111/j.1365-2699.2004.01073.x>, 2004.

1068 McCallum, I., Obersteiner, M., Nilsson, S., and Shvidenko, A.: A spatial comparison of four satellite
1069 derived 1km global land cover datasets, Int. J. Appl. Earth Observ., 8, 246-255,
1070 <https://doi.org/10.1016/j.jag.2005.12.002>, 2006.

1071 Meng, Z., Dong, J., Ellis, E. C., Metternicht, G., Qin, Y., Song, X.-P., Löfqvist, S., Garrett, R. D., Jia, X.,
1072 and Xiao, X.: Post-2020 biodiversity framework challenged by cropland expansion in protected areas,
1073 Nature Sustainability, <https://doi.org/10.1038/s41893-023-01093-w>, 2023.

1074 Meyer, M. F., Labou, S. G., Cramer, A. N., Brousil, M. R., and Luff, B. T.: The global lake area, climate,
1075 and population dataset, Sci. Data, 7, 174, <https://doi.org/10.1038/s41597-020-0517-4>, 2020.

1076 Moody, A. and Woodcock, C.: Scale-dependent errors in the estimation of land-cover proportions:
1077 Implications for global land-cover datasets, Photogramm. Eng. Remote Sens., 60, 585-594, 1994.

1078 Pekel, J. F., Cottam, A., Gorelick, N., and Belward, A. S.: High-resolution mapping of global surface
1079 water and its long-term changes, Nature, 540, 418-422, <https://doi.org/10.1038/nature20584>, 2016.

1080 Pengra, B. W., Stehman, S. V., Horton, J. A., Dockter, D. J., Schroeder, T. A., Yang, Z., Cohen, W. B.,

1081 Healey, S. P., and Loveland, T. R.: Quality control and assessment of interpreter consistency of annual
1082 land cover reference data in an operational national monitoring program, *Remote Sens. Environ.*, 238,
1083 111261, <https://doi.org/10.1016/j.rse.2019.111261>, 2020.

1084 Pickens, A. H., Hansen, M. C., Hancher, M., Stehman, S. V., Tyukavina, A., Potapov, P., Marroquin, B.,
1085 and Sherani, Z.: Mapping and sampling to characterize global inland water dynamics from 1999 to
1086 2018 with full Landsat time-series, *Remote Sens. Environ.*, 243, 111792,
1087 <https://doi.org/10.1016/j.rse.2020.111792>, 2020.

1088 Razi, S., Karami Mollaei, M. R., and Ghasemi, J.: A novel method for classification of BCI multi-class
1089 motor imagery task based on Dempster–Shafer theory, *Inf. Sci.*, 484, 14-26,
1090 <https://doi.org/10.1016/j.ins.2019.01.053>, 2019.

1091 Rottensteiner, F., Trinder, J. C., Clode, S., and Kubik, K.: Using the Dempster-Shafer method for the
1092 fusion of LIDAR data and multi-spectral images for building detection, *Inform. Fusion.*, 6, 283-300,
1093 <https://doi.org/10.1016/j.inffus.2004.06.004>, 2005.

1094 Running, S. W.: Ecosystem disturbance, carbon, and climate, *Science*, 321, 652-653,
1095 <https://doi.org/10.1126/science.1159607>, 2008.

1096 Schewe, J., Gosling, S. N., Reyer, C., Zhao, F., Ciais, P., Elliott, J., Francois, L., Huber, V., Lotze, H. K.,
1097 Seneviratne, S. I., van Vliet, M. T. H., Vautard, R., Wada, Y., Breuer, L., Büchner, M., Carozza, D. A.,
1098 Chang, J., Coll, M., Deryng, D., de Wit, A., Eddy, T. D., Folberth, C., Frieler, K., Friend, A. D., Gerten,
1099 D., Gudmundsson, L., Hanasaki, N., Ito, A., Khabarov, N., Kim, H., Lawrence, P., Morfopoulos, C.,
1100 Müller, C., Müller Schmied, H., Orth, R., Ostberg, S., Pokhrel, Y., Pugh, T. A. M., Sakurai, G., Satoh,
1101 Y., Schmid, E., Stacke, T., Steenbeek, J., Steinkamp, J., Tang, Q., Tian, H., Tittensor, D. P., Volkholz,
1102 J., Wang, X., and Warszawski, L.: State-of-the-art global models underestimate impacts from climate
1103 extremes, *Nat. Commun.*, 10, 1005, <https://doi.org/10.1038/s41467-019-08745-6>, 2019.

1104 See, L., Schepaschenko, D., Lesiv, M., McCallum, I., Fritz, S., Comber, A., Perger, C., Schill, C., Zhao,
1105 Y., Maus, V., Siraj, M. A., Albrecht, F., Cipriani, A., Vakolyuk, M. y., Garcia, A., Rabia, A. H., Singha,
1106 K., Marcarini, A. A., Kattenborn, T., Hazarika, R., Schepaschenko, M., van der Velde, M., Kraxner, F.,
1107 and Obersteiner, M.: Building a hybrid land cover map with crowdsourcing and geographically
1108 weighted regression, *ISPRS J. Photogramm.*, 103, 48-56,
1109 <https://doi.org/10.1016/j.isprsjprs.2014.06.016>, 2015.

1110 Shafizadeh-Moghadam, H., Minaei, M., Feng, Y., and Pontius, R. G.: GlobeLand30 maps show four
1111 times larger gross than net land change from 2000 to 2010 in Asia, *Int. J. Appl. Earth Observ.*, 78, 240-
1112 248, <https://doi.org/10.1016/j.jag.2019.01.003>, 2019.

1113 Shimada, M., Itoh, T., Motooka, T., Watanabe, M., Shiraiishi, T., Thapa, R., and Lucas, R.: New global
1114 forest/non-forest maps from ALOS PALSAR data (2007–2010), *Remote Sens. Environ.*, 155, 13-31,
1115 <https://doi.org/10.1016/j.rse.2014.04.014>, 2014.

1116 Song, X., Hansen, M. C., Stehman, S. V., Potapov, P. V., Tyukavina, A., Vermote, E. F., and Townshend,
1117 J. R.: Global land change from 1982 to 2016, *Nature*, 560, 639-643, <https://doi.org/10.1038/s41586-018-0411-9>, 2018.

1119 Sun, B., Chen, X., and Zhou, Q.: Uncertainty assessment of GlobeLand30 land cover data set over central
1120 Asia, *Int. Arch. Photogramm. Remote Sens. Spat. Inf. Sci.*, 41, 1313, <https://doi.org/10.5194/isprs-archives-XLI-B8-1313-2016>, 2016.

1122 Teluguntla, P., Thenkabail, P. S., Oliphant, A., Xiong, J., Gumma, M. K., Congalton, R. G., Yadav, K.,
1123 and Huete, A.: A 30-m landsat-derived cropland extent product of Australia and China using random
1124 forest machine learning algorithm on Google Earth Engine cloud computing platform, *ISPRS J.*

1125 Photogramm., 144, 325-340, <https://doi.org/10.1016/j.isprsjprs.2018.07.017>, 2018.

1126 Verburg, P. H., Neumann, K., and Nol, L.: Challenges in using land use and land cover data for global
 1127 change studies, *Glob. Change Biol.*, 17, 974-989, <https://doi.org/10.1111/j.1365-2486.2010.02307.x>,
 1128 2011.

1129 Verburg, P. H., Mertz, O., Erb, K.-H., Haberl, H., and Wu, W.: Land system change and food security:
 1130 towards multi-scale land system solutions, *Curr. Opin. Environ. Sustain.*, 5, 494-502,
 1131 <https://doi.org/10.1016/j.cosust.2013.07.003>, 2013.

1132 Wickham, J., Stehman, S. V., Sorenson, D. G., Gass, L., and Dewitz, J. A.: Thematic accuracy assessment
 1133 of the NLCD 2016 land cover for the conterminous United States, *Remote Sens. Environ.*, 257, 112357,
 1134 <https://doi.org/10.1016/j.rse.2021.112357>, 2021.

1135 Wu, J., Wang, X., Zhong, B., Yang, A., Jue, K., Wu, J., Zhang, L., Xu, W., Wu, S., Zhang, N., and Liu,
 1136 Q.: Ecological environment assessment for Greater Mekong Subregion based on Pressure-State-
 1137 Response framework by remote sensing, *Ecol. Indic.*, 117, 106521,
 1138 <https://doi.org/10.1016/j.ecolind.2020.106521>, 2020.

1139 Wulder, M. A., Li, Z., Campbell, E. M., White, J. C., Hobart, G., Hermosilla, T., and Coops, N. C.: A
 1140 national assessment of wetland status and trends for Canada's forested ecosystems using 33 years of
 1141 earth observation satellite data, *Remote Sensing*, 10, 1623, <https://doi.org/10.3390/rs10101623>, 2018.

1142 Xiong, J., Thenkabail, P. S., Tilton, J. C., Gumma, M. K., Teluguntla, P., Oliphant, A., Congalton, R. G.,
 1143 Yadav, K., and Gorelick, N.: Nominal 30-m cropland extent map of continental Africa by integrating
 1144 pixel-based and object-based algorithms Using Sentinel-2 and Landsat-8 data on Google Earth Engine,
 1145 *Remote Sensing*, 9, 1065, <https://doi.org/10.3390/rs9101065>, 2017.

1146 Xu, G., Zhang, H., Chen, B., Zhang, H., Yan, J., Chen, J., Che, M., Lin, X., and Dou, X.: A Bayesian
 1147 based method to generate a synergetic land-cover map from existing land-cover products., *Remote*
 1148 *Sensing*, 6, 5589-5613, <https://doi.org/10.3390/rs606558910.3390/rs6065589>, 2014.

1149 Xue, J., Wang, Y., Teng, H., Wang, N., Li, D., Peng, J., Biswas, A., and Shi, Z.: Dynamics of vegetation
 1150 greenness and lits response to climate change in Xinjiang over the past two decades, *Remote Sensing*,
 1151 13, 4063, <https://doi.org/10.3390/rs13204063>, 2021.

1152 Yang, J. and Huang, X.: The 30 m annual land cover dataset and its dynamics in China from 1990 to
 1153 2019, *Earth Syst. Sci. Data*, 13, 3907-3925, <https://doi.org/10.5194/essd-13-3907-2021>, 2021.

1154 Yang, J., Gong, P., Fu, R., Zhang, M., Chen, J., Liang, S., Xu, B., Shi, J., and Dickinson, R.: The role of
 1155 satellite remote sensing in climate change studies, *Nat. Clim. Chang.*, 3, 875-883,
 1156 <https://doi.org/10.1038/nclimate1908>, 2013.

1157 Yang, L., Jin, S., Danielson, P., Homer, C., Gass, L., Bender, S. M., Case, A., Costello, C., Dewitz, J.,
 1158 Fry, J., Funk, M., Granneman, B., Liknes, G. C., Rigge, M., and Xian, G.: A new generation of the
 1159 United States National Land Cover Database: Requirements, research priorities, design, and
 1160 implementation strategies, *ISPRS J. Photogramm.*, 146, 108-123,
 1161 <https://doi.org/10.1016/j.isprsjprs.2018.09.006>, 2018.

1162 Yang, Y., Xiao, P., Feng, X., and Li, H.: Accuracy assessment of seven global land cover datasets over
 1163 China, *ISPRS J. Photogramm.*, 125, 156-173, <https://doi.org/10.1016/j.isprsjprs.2017.01.016>, 2017.

1164 Yu, L., Wang, J., Clinton, N., Xin, Q., Zhong, L., Chen, Y., and Gong, P.: FROM-GC: 30 m global
 1165 cropland extent derived through multisource data integration, *Int. J. Digit. Earth*, 6, 521-533,
 1166 <https://doi.org/10.1080/17538947.2013.822574>, 2013.

1167 Zhang, C., Dong, J., and Ge, Q.: Quantifying the accuracies of six 30-m cropland datasets over China: A
 1168 comparison and evaluation analysis, *Comput. Electron. Agric.*, 197, 106946,

1169 <https://doi.org/10.1016/j.compag.2022.106946>, 2022.

1170 Zhang, M., Ma, M., De Maeyer, P., and Kurban, A.: Uncertainties in classification system conversion
1171 and an analysis of inconsistencies in global land cover products, *ISPRS Int. J. Geo Inf.*, 6, 112,
1172 <https://doi.org/10.3390/ijgi6040112>, 2017.

1173 Zhang, X., Liu, L., Chen, X., Gao, Y., Xie, S., and Mi, J.: GLC_FCS30: global land-cover product with
1174 fine classification system at 30 m using time-series Landsat imagery, *Earth Syst. Sci. Data*, 13, 2753-
1175 2776, <https://doi.org/10.5194/essd-13-2753-2021>, 2021.

1176 Zhang, X., Liu, L., Zhao, T., Chen, X., Lin, S., Wang, J., Mi, J., and Liu, W.: GWL_FCS30: a global 30
1177 m wetland map with a fine classification system using multi-sourced and time-series remote sensing
1178 imagery in 2020, *Earth Syst. Sci. Data*, 15, 265-293, <https://doi.org/10.5194/essd-15-265-2023>, 2023.

1179 Zhang, X., Long, T., He, G., Guo, Y., Yin, R., Zhang, Z., Xiao, H., Li, M., and Bo, C.: Rapid generation
1180 of global forest cover map using Landsat based on the forest ecological zones, *J. Appl. Rem. Sens.*,
1181 14, 022211, <https://doi.org/10.1117/1.JRS.14.022211>, 2020.

1182 Zhao, J., Yu, L., Liu, H., Huang, H., Wang, J., and Gong, P.: Towards an open and synergistic framework
1183 for mapping global land cover, *PeerJ*, 9, e11877, <https://doi.org/10.7717/peerj.11877>, 2021.

1184 Zheng, W., Liu, Y., Yang, X., and Fan, W.: Spatiotemporal variations of forest vegetation phenology and
1185 its response to climate change in northeast China, *Remote Sensing*, 14, 2909,
1186 <https://doi.org/10.3390/rs14122909>, 2022.

1187